



1 **Analysis and evaluation of WRF microphysical schemes**  
2 **for deep moist convection over Southeastern South**  
3 **America (SESA) using microwave satellite observations**  
4 **and radiative transfer simulations**

5 **Victoria Sol Galligani<sup>1,2</sup>, Die Wang<sup>3</sup>, Milagros Alvarez Imaz<sup>1,2</sup>, Paola Salio<sup>1,2,4</sup>,**  
6 **and Catherine Prigent<sup>3</sup>**

7 <sup>1</sup>Centro de Investigaciones del Mar y la Atmsfera, CONICET-UBA, Buenos Aires, Argentina.

8 <sup>2</sup>UMI-Instituto Franco Argentino sobre Estudios del Clima y sus Impactos, Buenos Aires, Argentina.

9 <sup>3</sup>Laboratoire d'Etudes du Rayonnement et de la Matire en Astrophysique (LERMA), CNRS, Observatoire  
10 de Paris, Paris, France.

11 <sup>4</sup>Departamento de Ciencias de la Atmsfera y los Ocanos. FCEN. Universidad de Buenos Aires. Buenos  
12 Aires, Argentina.



## 13 Abstract

14 In the present study, three meteorological events of extreme deep moist convection,  
15 characteristic of South Easter South America, are considered to conduct a systematic  
16 evaluation of the microphysical parametrizations available in the Weather Research and  
17 Forecasting (WRF) model by undertaking a direct comparison between satellite-based  
18 simulated and observed microwave radiances. A research radiative transfer model, the  
19 Atmospheric Radiative Transfer Simulator (ARTS), is coupled with the Weather Research  
20 and Forecasting (WRF) model under three different microphysical parametrizations (WSM6,  
21 WDM6 and Thompson schemes). Microwave radiometry has shown a promising ability  
22 in the characterization of frozen hydrometeors. At high microwave frequencies, however,  
23 frozen hydrometeors significantly scatter radiation, and the relationship between radi-  
24 ation and hydrometeor populations becomes very complex. The main difficulty in mi-  
25 crowave remote sensing of frozen hydrometeor characterization is correctly characteriz-  
26 ing this scattering signal due to the complex and variable nature of the size, composi-  
27 tion and shape of frozen hydrometeors. The present study further aims at improving the  
28 understanding of frozen hydrometeor optical properties characteristic of deep moist con-  
29 vection events in South Easter South America. In the present study, bulk optical prop-  
30 erties are computed by integrating the single scattering properties of the Liu (2008) DDA  
31 single scattering database across the particle size distributions parametrized by the dif-  
32 ferent WRF schemes in a consistent manner, introducing the equal-mass approach. The  
33 equal mass approach consists in describing the optical properties of the WRF snow and  
34 graupel hydrometeors with the optical properties of habits in the DDA database whose  
35 dimensions might be different ( $D_{max}$ ) but whose mass is conserved. The performance  
36 of the radiative transfer simulations is evaluated by comparing the simulations with the  
37 available coincident microwave observations up to 190 GHz (with observations from TMI,  
38 MHS, and SSMI/S) using the Chi-square test. Good agreement is obtained with all ob-  
39 servations provided special care is taken to represent the scattering properties of the snow  
40 and graupel species.

## 41 1 Introduction

42 The continental region east of the Andes, covering the south of Brazil, Paraguay,  
43 Uruguay, and the north and centre of Argentina (usually referred to as South Eastern  
44 South America, SESA), is known for its large and intense Mesoscale Convective Systems  
45 (MCSs) within which severe weather events develop (e.g., *Altinger de Schwarzkopf and*  
46 *Necco* [1988], *Silva Dias* [2011], *Mezher and Barros* [2012], *Goodman et al.* [2013], *Salio*  
47 *et al.* [2015]). These are the regions where the strongest MCSs on Earth occur [*Zipsper*  
48 *et al.*, 2006]. In this data sparse region, little is known about the aspects of these sys-  
49 tems, including what governs their structure, life cycle, similarities and differences with  
50 severe weather-producing systems observed elsewhere on the Earth, and their predictabil-  
51 ity from minutes to climate time-scales. High resolution models are a powerful tool to  
52 study convection.

53 NWP models can be used to perform numerical experiments in controlled environ-  
54 mental conditions, to assess the impact of different physical processes and environmen-  
55 tal conditions upon the life cycle and the organization of convection (e.g., *Morrison and*  
56 *Khvorostyanov* [2005], among others). The description of cloud processes and ultimately  
57 the dynamical processes that result from numerical models need to be improved to more  
58 accurately describe key factors such as hydrometeor characteristics, latent heating prop-  
59 erties, radiative fluxes and forcing, entrainment, and cloud updraft and downdraft prop-  
60 erties. This is particularly important since, with the increase of computing power in the  
61 recent years, the physical parameterizations in climate and numerical weather predic-  
62 tion (NWP) models have improved to incorporate microphysical processes, often at in-  
63 creasingly high resolution, resolving the dynamical interactions in convective systems.



64 Cloud resolving models can be operated with different parameterizations, includ-  
65 ing different microphysics schemes. In recent years, increasingly detailed bulk cloud mi-  
66 crophysics parameterizations have been incorporated into cloud resolving models. Bulk  
67 microphysics represent the size spectra of the different hydrometeor species with a par-  
68 ticle size distribution function. In this way, microphysics parameterizations predict the  
69 development of one or more hydrometeor categories, their interactions and growth, and  
70 precipitation. Microphysics schemes may differ in the number of predicted species, pre-  
71 dicted moments, number of simulated microphysical processes, assumptions regarding  
72 the mass-size relationships and size-terminal fall speed relationships, and the assumed  
73 particle size distributions. An extensive evaluation of the existing schemes is needed in  
74 order to constrain and reduce the uncertainties associated with the parameterizations.  
75 The microphysical properties (e.g., dielectric properties, density, particle size distribu-  
76 tion, shape, orientation) of the frozen particles specifically, have a very complex tempo-  
77 ral and spatial variability, and lack robust parameterizations.

78 Microwave radiometry has shown a promising ability in the characterization of frozen  
79 particles, as it is able to penetrate and provide insight into the vertical profiles of most  
80 clouds, in contrast to infrared and visible observations, which essentially sense cloud tops.  
81 At low microwave frequencies, hydrometeors essentially interact with the radiation through  
82 emission and absorption. These interactions are well parameterized using only simple  
83 assumptions. In contrast, at high microwave frequencies, frozen hydrometeors can sig-  
84 nificantly scatter radiation, and the relationship between radiation and hydrometeor pop-  
85 ulations becomes much more complex. In the model-to-satellite approach, satellite ra-  
86 diances are simulated using outputs from atmospheric models and compared to avail-  
87 able observations using a radiative transfer model (e.g. *Chaboureau et al.* [2008]; *Meirol-  
88 Mautner et al.* [2007], *Galligani et al.* [2014]). Under cloudy conditions and at high mi-  
89 crowave frequencies (> 80 GHz), the radiative transfer calculations are more difficult to  
90 handle and they strongly depend upon a much more detailed description of the cloud  
91 microphysics than the parameterizations that are currently available in NWP models.

92 In the present study, meteorological events of extreme deep moist convection are  
93 considered to conduct a systematic evaluation of the micro-physical parametrizations avail-  
94 able in the Weather Research and Forecasting (WRF) model. In order to do this, a di-  
95 rect comparison between satellite-based simulated and observed microwave radiances is  
96 proposed by coupling the WRF model with a research radiative transfer model, the At-  
97 mospheric Radiative Transfer Simulator (ARTS). Since the simulation of passive microwave  
98 radiances requires good knowledge of the scattering properties of frozen hydrometeors,  
99 the present study further aims at improving the understanding of frozen hydrometeor  
100 optical properties and the characteristics of deep convection in the SESA region. This  
101 study is structured as follows. Section 2 introduces a particular deep moist convection  
102 event in the SESA region, together with a description of the models used and the avail-  
103 able microwave observations. This section includes a discussion of the modelling system  
104 developed in the present study that converts WRF outputs to simulated microwave bright-  
105 ness temperatures (TBs). Section 3 focuses on the difficulties associated with providing  
106 the radiative transfer model used with a rather accurate description of the radiative prop-  
107 erties of the hydrometeors modelled by WRF, especially for frozen hydrometeors. A sen-  
108 sitivity study of the passive radiative transfer simulations to the hydrometeor charac-  
109 teristics is presented in Section 4 for specific observed transects, followed by a statisti-  
110 cal analysis of the simulated and observed brightness temperature distributions. Section  
111 5 further tests the drawn conclusions by simulating two other convective events in the  
112 region. Finally, Section 6 presents the conclusions and details future work being carried  
113 out to exploit this modelling system.



114 **2 A severe weather event associated with deep convection in the SESA**  
115 **region: models and observations**

116 The focus of the present study is an intense MCS event observed over the centre  
117 of Argentina on 6 December 2012. On the 6 and 7 of December, the center of Argentina  
118 was affected by many severe weather events, including tornadoes, winds above 100 km/hr,  
119 and intense precipitation that caused tragic floods in the city of Buenos Aires. The fol-  
120 lowing sub-sections describe the observations available during this meteorological event,  
121 the configuration used in the WRF model runs and its microphysics parameterizations,  
122 and the radiative transfer model used.

123 **2.1 Coincident satellite observations**

124 For the MCS event on the 6 December 2012 there are coincident observations avail-  
125 able from the Tropical Rainfall Measuring Mission (TRMM) at 07:00 UTC and the Mi-  
126 crowave Humidity Sounder (MHS) onboard NOAA-19 at 19:00 UTC. TRMM carries a  
127 suite of instruments designed to study precipitation in the tropics (Kummerow *et al.* [1998]).  
128 The TRMM Microwave Imager (TMI) is a conical imager operating at 10.7, 19.4, 21.3,  
129 37, and 85.5 GHz with a 53° incidence angle. It has two orthogonal polarizations (ex-  
130 cept at 22 GHz) and spatial resolutions between 63 km x 37 km, and 7km x 5km, de-  
131 pending on the channel. It covers a swath of 780 km. The TRMM Precipitation Radar  
132 (PR) operates at 13.8 GHz with a 4 km resolution and a swath of 220 km. The swath  
133 is located in the center of the TMI swath. The Microwave Humidity Sounder (MHS) is  
134 a cross-track sounder with surface zenith angles varying between 0° and 58°. The chan-  
135 nels are located at 89.0, 157.0, 183.3 ± 1, 183.3 ± 3 and 190.3 GHz. The channels near  
136 the water vapour line of 183.3 GHz are strongly sensitive to atmospheric absorption, in  
137 contrast to the more transparent window channels at 89, 157 and 190 GHz. The spatial  
138 resolution at nadir is 16 km for all channels and increases away from nadir (26 km at  
139 the furthest zenith angle along track). The polarization state for each channel is a com-  
140 bination between the two orthogonal linear polarizations (V and H), where the polar-  
141 ization mixing depends on the scanning angle. TMI observations at 10.7, 19.4, 37 and  
142 85.5 GHz are shown in Figure 1(a-d) for vertical (V) polarizations only. The highly scat-  
143 tering MCS event is evidenced by brightness temperature depressions at the higher fre-  
144 quency channels (> 37 GHz). At the lower frequency channels (< 37 GHz), TMI is mostly  
145 sensitive to surface emission. The ocean surface emissivities are rather low and polar-  
146 ized, contrarily to land surfaces that usually have a high emissivity with limited polar-  
147 ization. For low atmospheric opacity at the lower frequencies, the contrast between ocean  
148 and land is larger. This contrast can easily be seen up to 19 GHz in Figure 1. At 37 GHz,  
149 both liquid water emission in clouds and frozen hydrometeor scattering induce a decrease  
150 in TB over the highly emitting land. At the higher frequency channel of 85.5 GHz, cloud  
151 structures appear cold due to the strong scattering of frozen hydrometeors, with rather  
152 low TBs (down to almost 50 K on this case study). Figure 1(e) shows the PR reflectiv-  
153 ity and the PR retrieved freezing level height crossing the MCS system along the black  
154 line shown in Figure 1(d). MHS observations at 89, 157, 183 ± 1 and 190 GHz are shown  
155 in Figure 2(a-d) (the 183 ± 3 is very similar to the 190 GHz channel and is not shown).  
156 Note that MHS zenith angles vary between 58° (on the west) and 0° (on the east). In  
157 the window channels, the observations over the ocean present rather low brightness tem-  
158 peratures due to the low ocean emissivity when compared to those over the continen-  
159 tal region. With increasing atmospheric opacity in the H<sub>2</sub>O water vapor line, as evidenced  
160 at 183 ± 1 GHz, the contrast between land and ocean disappears. In the window chan-  
161 nels, the scattering effect due to the presence of convection can be observed from the bright-  
162 ness temperatures depressions that increase with frequency, especially in the window chan-  
163 nels. The strong brightness temperature depressions that are even observed in the wa-  
164 ter vapour line channel (TBs ≈ 100 K) evidence the presence of highly scattering clouds.  
165 The following subsections described the models exploited to use this meteorological event  
166 in a systematic evaluation of microphysical parameterizations.



167 **2.2 The mesoscale cloud model: The Weather Research and Forecast-**  
168 **ing (WRF) model and the WSM6, WDM6 and THOM microphysics**  
169 **options**

170 WRF is a non-hydrostatic mesoscale numerical weather prediction system designed  
171 for both atmospheric research and operational forecasting needs. It provides a full de-  
172 scription of the atmospheric parameters (pressure, temperature, and mixing ratios for  
173 the water vapor, and the five hydrometeor categories). In the present study, WRF-ARW  
174 (*Skamarock and Klemp [2008]*) version 3.6 is used for the model simulations consider-  
175 ing only one domain with 4 km grid spacing and 38 vertical levels. The model was ini-  
176 tialized with GFS (Global Forecast System) initial conditions of 0.5° resolution at 00:00  
177 UTC for 6 December 2012. The model was integrated up to 36 hours with every 3 hour  
178 updates of the boundary conditions taken from GFS analysis also at 0.5° resolution. Fig-  
179 ure 3 shows the domain considered and Table 1 presents the different parametrizations  
180 used in the model run.

181 The three microphysics schemes used in the present study include the WRF Single-  
182 Moment 6 (WSM6; *Hong and Lim [2006]*), the WRF Double-Moment 6 (WDM6; *Hong*  
183 *et al. [2010]*) and the Thompson schemes (THOM, *Thompson et al. [2008]*). The three  
184 schemes have the same number of water species (water vapour, cloud water, rainwater,  
185 cloud ice, snow, and graupel). The WSM6 is a single-moment scheme that prognoses the  
186 mass mixing ratio of species, whereas the WDM6 is a double moment scheme based on  
187 the WSM6 that additionally prognoses the number concentration mixing ratios of cloud  
188 water and rainwater related to the size distribution of the species, i.e., double-moment  
189 representation of warm-rain. The THOM scheme also additionally prognoses number con-  
190 centration mixing ratios for cloud ice and warm-rain.

191 These microphysics schemes generally assume a gamma particle size distribution  
192 (PSD) for precipitating hydrometeor species of the form:

$$N_x(D) = \int N_{0x} D^{\mu_x} e^{-\lambda_x D} dD, \quad (1)$$

193 where  $N_x(D)$  represents the number concentration ( $\text{m}^{-1}\text{m}^{-3}$ ) of particles of a given  
194 hydrometeor class ( $x$ ) and diameter  $D$ ,  $N_{0x}$  is the  $y$ -intercept parameter,  $\lambda_x$  is the slope  
195 parameter, and  $\mu_x$  is the shape parameter of the distribution. This gamma distribution  
196 is simplified to an exponential distribution by setting  $\mu_x$  to zero for rainwater, snow, and  
197 graupel in both the WSM6 and WDM6 schemes, and for rainwater and graupel in the  
198 THOM scheme. Snow is unique in the THOM scheme because, in contrast to most WRF  
199 bulk schemes, its particle size distribution is not an exponential size distribution, but  
200 a sum of two gamma functions following observations by *Field et al. [2005]*. The particle  
201 size distribution, hereafter referred to as the *Field et al. [2005]* size distribution, is  
202 based on in-situ observations valid for tropical and midlatitude clouds, and has been used  
203 with positive results in recent validation studies (e.g. *Doherty et al. [2007]*; *Kulie et al.*  
204 *[2010]*). Additionally, snow mass (and indirectly density) in the THOM scheme is not  
205 fixed and varies inversely with diameter  $D$  as  $m(D)=0.069D^2$ , unlike most schemes, in-  
206 cluding the WSM6 and WDM6 schemes, that have a fixed mass determined by  $m(D)=(\rho_s\pi/6)D^3$   
207 where  $\rho_s=0.1\text{kg/m}^3$ . This is an important difference since observational studies rarely  
208 support fixed density snow habits. *Magono [1965]* and many later studies recognize that  
209 a size-independent density is not a physically sound assumption for snowflakes because  
210 of the rigidity of ice and the nature of the snow formation processes (*Leimonen et al. [2012]*).  
211 The *Field et al. [2005]* PSD takes into account the parameters of the mass-size relation-  
212 ship and predicts a higher number of smaller particles, but a smaller number of larger  
213 particles than the WSM6/WDM6 schemes. It is also worth stating that the graupel species  
214 in the THOM scheme represent rimed ice (e.g., hybrid like graupel–hail category) by



215 using a two-parameter diagnostic dependence of its size distribution intercept param-  
216 eter based on the mass mixing ratio and amount of supercooled liquid water.

217 Figure 4 shows the integrated column contents in  $\text{kg/m}^2$  for rain (4a-c), snow (4d-  
218 f) and graupel (4g-i), as simulated by the three different schemes at 19:00 UTC with a  
219 minimum threshold of  $0.05 \text{ kg/m}^2$ . Note that the integrated contents for ice cloud and  
220 cloud water are not shown. This specific time output corresponds to the over-pass of the  
221 Microwave Humidity Sounder (MHS) discussed above. Another time output considered  
222 in the present study is the TRMM overpass at 07:00 UTC (not shown). The black line  
223 in Figure 4g represents an MHS transect simulated which is explored in Section 4. A first  
224 look at Figure 4 shows that the three schemes model the structure and the location of  
225 the cloud system fairly similarly. The brightness temperature depressions observed in  
226 Figure 2 (and Figure 1) correspond to the cloud structures simulated by WRF in Fig-  
227 ure 4 at 19:00 UTC (and at 07:00 UTC not shown). A close examination of MHS ob-  
228 servations (Figure 2) and the WRF cloud outputs (Figure 4), however, reveals that the  
229 cloud system modelled by WRF is slightly time lagged and misplaced with respect to  
230 the observations, similarly to TMI observations (Figure 1) and the corresponding WRF  
231 cloud outputs (not shown). A closer look at the mass loading of the different hydrom-  
232 eteor also evidences a strong sensitivity to the microphysical scheme used. As expected,  
233 the WSM6 and the WDM6 schemes model similar hydrometeor mass loadings. The THOM  
234 scheme, on the other hand, shows much higher snow contents. Figure 5 further shows  
235 the domain-averaged vertical distribution of the hydrometeor contents modelled by the  
236 different schemes between 18:00 and 19:00 UTC. Units are in  $\text{g/kg}$  for all the species.  
237 Both Figure 4 and Figure 5 show a comparable behaviour in the frozen phase (ice, snow  
238 and graupel) in the WSM6 and WDM6 schemes. This is expected because the WDM6  
239 scheme follows the cold-rain processes of the WSM6 scheme and the added processes in  
240 the WDM6 do not affect the frozen phases directly (*Lim and Hong* [2010]). Figure 5 shows  
241 an increase of the WDM6 rainwater mixing ratio below 5 km with less cloud droplet mix-  
242 ing ratios. The THOM scheme, as previously reported by e.g., *Kim et al.* [2013], is dom-  
243 inated by snow throughout the vertical profile and predicts the smallest amount of rain  
244 water. The THOM scheme has a maximum cloud water content between 8 and 10 km.  
245 This peak of enhanced cloud water content is found within and around strong convec-  
246 tive updrafts. In order to compare the distribution of the frozen hydrometeor species among  
247 the total frozen phase for each scheme, Figure 5 additionally shows the mean vertical  
248 profile of the total frozen content (i.e., ice+snow+graupel, shown in light blue). The to-  
249 tal frozen content is comparable in magnitude in all the schemes analyzed but since each  
250 scheme has different intrinsic assumed characteristics and microphysical processes, they  
251 partition the total content in different ways between graupel, cloud ice, and snow. The  
252 THOM scheme has the most prominent vertical structure. Note that very similar remarks  
253 can be drawn from the model simulations at 07:00 UTC in coincidence with the avail-  
254 able TMI observations (not shown).

### 255 2.3 The radiative transfer model: The atmospheric radiative transfer 256 simulator (ARTS)

257 A robust radiative transfer model allows consistently modelling passive observa-  
258 tions when using (1) WRF outputs to describe the atmospheric profiles as discussed above  
259 and, (2) a rather accurate description of the radiative properties of the hydrometeors in  
260 each model grid point. In the present study, the Atmospheric Radiative Transfer Sim-  
261 ulator (ARTS, *Eriksson et al.* [2011]) is used. ARTS is a very flexible tool, capable of  
262 modeling different atmospheric conditions and different sensor configurations. ARTS is  
263 an open-source code available at <http://www.radiativetransfer.org> along with extensive  
264 documentation. It is a well validated model (*Melsheimer et al.* [2005], *Buehler et al.* [2006],  
265 *Saunders et al.* [2007]) and it can handle scattering with arbitrary complex scattering  
266 properties set by the users. It provides a Monte Carlo module to solve the radiative trans-



267 fer equation under cloudy conditions (*Davis et al.* [2007]) which takes full account of the  
268 3-D description of the atmospheric state modelled by the WRF outputs.

269 To accurately simulate real microwave observations of satellite-based instruments  
270 with ARTS a correct description of the surface properties, the observation geometry and  
271 the cloud optical properties is important. The proposed methodology involves a series  
272 of coupling tools. The Tool to Estimate Land Surface Emissivities from Microwave to  
273 Sub-millimeter waves (TELSEM2; *Wang et al.* [2016]) and the Tool to Estimate Sea Sur-  
274 face Emissivity from Microwave to Sub-millimeter waves (TESSEM2; *Prigent et al.* [2016])  
275 are used to determine land and ocean surface emissivities respectively. TELSEM2  
276 provides the emissivity (V and H components) for any location, any month, and any inci-  
277 dence angle with a spatial resolution of 0.25 degrees. TESSEM2 calculates sea surface emis-  
278 sivities from wind, sea surface temperature and viewing angle. Coupling WRF outputs  
279 with ARTS further requires a good description of the hydrometeor optical properties (i.e.,  
280 the single scattering properties) and particle size distributions. Bulk optical properties  
281 are computed by integrating the single scattering properties of particles across a given  
282 particle size distribution. The bulk optical properties of the hydrometeors at each model  
283 level have a strong influence on the radiative transfer equation for both passive and ac-  
284 tive simulations. The single scattering properties are determined by hydrometeor com-  
285 position, density, dielectric properties, size, shape and orientation. While the particle size  
286 distribution of species is intrinsic to each WRF microphysics scheme, cloud resolving mod-  
287 els like WRF do not determine all of the parameters needed to determine the single scat-  
288 tering properties, and further assumptions are necessary. This is discussed in more de-  
289 tail in Section 3 below.

### 290 3 Modelling the single scattering properties

291 Throughout the present study, the goal when implementing the single scattering  
292 properties and the particle size distribution of the hydrometeor species in ARTS is to  
293 remain as consistent as possible with the corresponding WRF microphysics scheme. The  
294 particle size distributions for each hydrometeor category in the radiative transfer sim-  
295 ulations remains consistent with the parameterizations used in the WRF. The single scat-  
296 tering properties of hydrometeors, on the other hand, require assumptions to be made.

297 For simplicity, the optical properties of cloud ice, cloud water and rain are held con-  
298 stant and represented by Mie spheres with the dielectric properties of *Liebe et al.* [1991]  
299 for liquid species and *Mätzler* [2006] for ice crystals. These are reasonable assumptions  
300 for the liquid phase. The mass loadings of ice crystals simulated by WRF in the scenes  
301 explored are negligible and, at the microwave frequencies analysed, small pure ice crys-  
302 tals produce very little scattering. Modelling snow and graupel species, on the other hand,  
303 is much more challenging, mainly due to uncertainties in their composition and shape.  
304 Frozen hydrometeors have a large spatial and temporal variability and are of a complex  
305 non-spherical nature. Frozen hydrometeors can be both single crystals (with shapes in-  
306 cluding needles, plates, columns, rosettes, dendrites, etc.) or aggregates (e.g., *Baran* [2012]).  
307 There is a highly complex mixture of differently shaped and sized habits in the atmo-  
308 sphere, and this mixture further varies with particle size. However, the only computa-  
309 tionally realistic approach is to assume a one-shape model to represent the total habit  
310 population even if this approach does not fully capture the large variability observed in  
311 nature.

312 There are a number of approaches used to model frozen hydrometeors. One is to  
313 assume that the habits have certain known realistic shapes like plates or rosettes, and  
314 calculate their single scattering properties using the Discrete Dipole Approximation method  
315 (DDA, *Draine and Flatau* [1994]). The second approach is to approximate these com-  
316 plex shapes with spheres with the same mass and apply Mie theory. This imaginary sphere  
317 can either be a pure ice sphere with a smaller diameter or a “soft sphere” of the same



318 size but with lower density and a reduced effective dielectric constant. In the soft sphere  
 319 approximation, particles are considered to be homogeneous mixtures of ice/air, or possi-  
 320 bly ice/air/liquid water. This approach requires that the mass fraction of, for exam-  
 321 ple air in the ice/air mixture and the corresponding dielectric properties of the homo-  
 322 geneous mixture, be determined. The soft sphere approximation has been widely used  
 323 together with the T-matrix method to model spheres and spheroids (e.g., *Galligani et al.*  
 324 [2014]), where the air fraction was either set to be fixed or derived from mass-size parametriza-  
 325 tions or snow habit densities. This approach, however, has been shown to be problem-  
 326 atic, as the air fraction in the mixing rule must be allowed to vary with both particle size  
 327 and frequency for a better fit (e.g., *Galligani et al.* [2014], *Eriksson et al.* [2015]). *Liu*  
 328 [2004] showed that the optimal softness parameter, or effective density, varies with fre-  
 329 quency. However, using density-based air fractions which are a function of frequency and  
 330 size is an unphysical approach. Furthermore, for large particles in the more realistic size  
 331 dependent mass parametrizations as in the THOM scheme, it has been observed that  
 332 the larger particles have high air fractions and consequently negligible scattering efficien-  
 333 cies (e.g., *Galligani et al.* [2014]). Although the DDA approach can accurately evaluate  
 334 the radiative properties of more realistic, complex shapes, choosing a particular shape  
 335 model remains arbitrary and hence problematic. Readers are encouraged to refer to *Eriks-*  
 336 *son et al.* [2015] for a detailed discussion on the microwave optical properties of ice hy-  
 337 drometeors.

338 In this study, snow and graupel hydrometeors are modelled using scattering prop-  
 339 erties of realistic snowflake habits from the *Liu* [2008] database. *Liu* [2008] used the DDA  
 340 code of *Draine and Flatau* [1994] to compute the single scattering properties of differ-  
 341 ently shaped ice crystals. The *Liu* [2008] database presents 11 different randomly ori-  
 342 ented ice crystals at 22 frequencies (3.0 - 340 GHz) and at 5 different temperatures (233,  
 343 243, 253, 263 and 273 K). The main properties of the database are listed in Table 2. The  
 344 soft sphere approximation is also used for comparison, and following the conclusions drawn  
 345 in *Eriksson et al.* [2015], the *Maxwell-Garnett* [1906] mixing rule for air in ice is used to  
 346 model the effective dielectric properties, as it appears to have the least deviation from  
 347 DDA scattering properties.

348 The snow and graupel contents are thus described by the corresponding WRF parti-  
 349 cle size distribution and their single scattering properties by the *Liu* [2008] database.  
 350 One last remark must be made when using the *Liu* [2008] database to describe the scat-  
 351 tering properties of snow and graupel consistently with the WRF microphysics param-  
 352 etrizations. Both the DDA habits and the WRF schemes use a mass-size relationship of  
 353 the form

$$m = aD_{max}^b, \quad (2)$$

354 where  $a$  and  $b$  are parameters intrinsic to each of the DDA habits in the *Liu* [2008] database  
 355 or each of the hydrometeor species in the microphysics schemes, and indirectly deter-  
 356 mine the habit density. As described in Section 2.2, the snow mass in the THOM scheme  
 357 is not fixed with size and follows  $m(D)=0.069D^2$  while the WSM6 and WDM6 schemes  
 358 have a constant mass value determined by  $m(D)=(\rho_s\pi/6)D^3$  where  $\rho_s=0.1\text{kg/m}^3$ . Graupel  
 359 species in the WSM6, WDM6 and THOM schemes have a constant density of  $\rho_g=0.4\text{kg/m}^3$   
 360 and follow  $m(D)=(\rho_g\pi/6)D^3$ . Similarly, each of the *Liu* [2008] habits are described by  
 361 different  $a$  and  $b$  parameters listed in Table 2. In order to consistently simulate WRF  
 362 model outputs with the *Liu* [2008] habits, the approach used in the present study is to  
 363 assume an equal mass habit where

$$a_{WRF}D_{max}^{b_{WRF}} = a_{LIU}D_{max}^{b_{LIU}}. \quad (3)$$

364 In Equation 3,  $D_{max}$  is inferred from WRF parametrizations and is used in the parti-  
 365 cle size distribution.  $D_{max}$  is the corresponding equal mass DDA habit size used to de-  
 366 scribe the scattering properties of the WRF species consistently. This discussion is im-  
 367 portant since particle size is a key parameter in single scattering calculations. Figures



368 6(a) and (b) shows the corresponding equal mass  $D'_{max}$  for a selected number of *Liu* [2008]  
369 habits when using the WSM6/WDM6 and THOM schemes respectively. The choice of  
370 DDA habits shown is a result of regrouping certain habits that behave similarly, such  
371 as the Thin hexagonal column, the Long hexagonal column, the Short hexagonal column  
372 and the Thick hexagonal column, or the bullet rosettes. Note that the included black  
373 dashed line represents unity. As shown in Figures 6(a) and 6(b), for a given maximum  
374 particle dimension in WRF, the equal mass DDA habit  $D'_{max}$  can be very different for  
375 each of the *Liu* [2008] habits. Figures 6(a) and 6(b) also show that equal mass DDA habit  
376  $D'_{max}$  is larger when using the WSM6 and WDM6 schemes than when using the THOM  
377 scheme. This is expected due to the intrinsic  $\rho_s$  differences in these schemes. For the most  
378 compact habits of the DDA database, like columns and plates, the difference between  
379 the WSM6/WDM6 and the THOM schemes is the smallest, while the largest differences  
380 are seen for the dendrite and sector habits. The thin hexagonal plates for example, have  
381  $D'_{max}$  diameters above  $D_{max}$  for the WSM6/WDM6, and  $D'_{max}$  diameters below  $D_{max}$   
382 in the THOM scheme. The 6-b rosette  $D'_{max}$  is larger for the WSM6/WDM6 schemes  
383 but close to unity for the THOM scheme.

384 The bulk scattering properties (e.g., the extinction coefficient  $\beta_e$ ) of each of the *Liu*  
385 [2008] habits are shown in Figures 6(c) as a function of snow water content at 150 GHz  
386 for the WSM6/WDM6 and the *Field et al.* [2005] snow particle size distributions. This  
387  $\beta_e$  parameter is calculated by integrating the extinction cross section  $\sigma_e(D)$  across the  
388 particle size distribution  $N(D)$ :

$$\beta_e = \int_0^{\infty} \sigma_e(D)N(D)dD. \quad (4)$$

389 As expected, extinction (and scattering) increases with frequency (not shown) and snow  
390 water content. Not shown is the asymmetry parameter which gives an overall descrip-  
391 tion of the phase function, i.e., the angular redistribution of scattered radiation. In con-  
392 trast to the *Liu* [2008] habits, the low density Mie sphere model (not shown) gives very  
393 strong forward scattering for high snow water contents. The *Liu* [2008] habits produce  
394 more balanced forward and backward scattering. Although not shown graphically, analysing  
395 the sensitivity of these bulk scattering properties with frequency indicates that these con-  
396 clusions are broadly true for the microwave range of interest in the present study. As the  
397 scattering increases, so do the differences between the bulk WSM6/WDM6 and THOM  
398 properties. The integrated bulk properties showed in Figure 6(c) include the effects of  
399 using the equal mass habit approach discussed above. Both the particle size distribu-  
400 tions and how  $D'_{max}$  differs from  $D_{max}$  play an important role. Figure 6(c) illustrates  
401 the complex nature of evaluating the relative importance of these two effects. In the WSM6/WDM6  
402 schemes, the thin hexagonal plates and the 6-b rosette are the most scattering habits,  
403 while the 6-b rosette and the dendrite habits are the least scattering habits. The bulk  
404 scattering properties using the WSM6 and WDM6 schemes lead to higher scattering than  
405 when using the THOM scheme, specially for the the most compact particles like columns  
406 and plates, which are the most scattering. The opposite is true with the less compact  
407 dendrite habits.

#### 408 4 Comparison of the simulations with coincident observations

409 The objective of the following radiative transfer simulations is to consistently simu-  
410 late the brightness temperature depressions observed related to the frozen phase us-  
411 ing WRF microphysical properties and the necessary additional assumptions, with the  
412 aim of evaluating the different DDA habits and the WRF microphysics options for the  
413 meteorological event described in Section 2. It is not to simulate the detailed spatial struc-  
414 ture of the observations because, as seen by comparing Figure 2 and Figure 4, there are  
415 differences in the location of the observed and modelled cloud system. This section pro-  
416 poses to undertake a sensibility analysis of the compatibility of WRF outputs and its  
417 intrinsic microphysics parametrizations with the *Liu* [2008] DDA habits. The present



418 study does not aim to search for the ‘best’ Liu habit. As discussed in the previous sec-  
419 tions, the radiative transfer simulations to be discussed depend mainly on (1) the inte-  
420 grated species content modelled by WRF, (2) the microphysics parametrized in each WRF  
421 scheme, and (3) the additional single scattering properties of the frozen phase, more specif-  
422 ically of snow species and graupel as discussed in Section 3. The particle size distribu-  
423 tion remains consistent to the WRF microphysics scheme of interest, unless specified oth-  
424 erwise.

425 To focus on cloudy simulations, one must first achieve robust clear sky simulations.  
426 For a quantitative comparison, the statistical distribution of the simulated and observed  
427 brightness temperatures is evaluated for some selected channels of TMI (10V, 19V, 22V,  
428 37V, 85V GHz) and MHS (157, 89 and  $183 \pm 1$  GHz). The statistical distributions (not  
429 shown) show a good agreement with the observed brightness temperatures under clear  
430 sky conditions, confirming the reliability of the radiative transfer simulation inputs (e.g.,  
431 the surface emissivity estimates used or the state of the atmosphere simulated by WRF).  
432 For the highly surface sensitive 19 GHz channel and the water vapour sensitive 22 GHz  
433 channel, good agreement is found for the WSM6, WDM6, and THOM schemes, with bi-  
434 ases (observed-simulated) of approximately -3.55 K and 0.6 K respectively over land. For  
435 the water vapour channel in MHS at  $183 \pm 1$  GHz, the schemes used show biases between  
436 -1.33 and -1.68 K over land. The analysis of the distributions of simulated and observed  
437 brightness temperatures under both clear and cloudy conditions, specially in window chan-  
438 nels, essentially shows that the largest differences between the observed and simulated  
439 brightness temperatures and especially at higher frequencies, is located in the lower end  
440 of the brightness temperature histograms where scattering is important. Characteris-  
441 ing the scattering signal responsible for the largest brightness temperature differences  
442 is the focus of the present study.

443 Figure 7 shows the WSM6, WDM6 and THOM simulated brightness temperatures  
444 at 19V, 37V and 85V GHz for a specific TMI scan of the observations presented in Fig-  
445 ure 1 for the 6th December at 7 UTC, at the initiation stages of the system. Figure 7  
446 shows the brightness temperature simulations for the selected Liu [2008] DDA habits in  
447 Figure 6. The bottom row of Figure 7 shows the corresponding integrated snow, grau-  
448 pel and rain contents simulated by the different WRF schemes. The out-most right col-  
449 umn shows the corresponding TMI observations and serves as a reference to analyse the  
450 simulations.

451 As discussed above, the clear sky observations are well simulated by all schemes.  
452 However, the simulation of brightness temperatures in the presence of high snow and/or  
453 graupel contents is shown to be problematic. This is clearly evidenced in Figure 7 by the  
454 large spread in the simulated brightness temperatures throughout the different schemes  
455 and the different DDA habits used. As expected, Figure 7 shows that the higher the fre-  
456 quency, the larger the brightness depression simulated and the larger the sensitivity to  
457 the different DDA habits. The large sensitivity of the simulated TBs to the DDA habits  
458 shown in Figure 7, illustrates how problematic the representation of snow/graupel scat-  
459 tering can be. Excessive scattering means that WRF generates more snow than is ob-  
460 served, that the radiative transfer model (and its necessary assumptions) simulates ex-  
461 cessive scattering, or both.

462 At 10 GHz (not shown), there is little sensitivity to scattering, and the most promi-  
463 nent feature is a strong brightness temperature drop at approximately  $-32.9^\circ$  due to a  
464 lake in central Uruguay. This is observed more prominently in simulations and not in  
465 observations due to the simplified antenna pattern used in the simulations. Due to the  
466 lack of sensitivity to scattering, there is little sensitivity to the different DDA habits or  
467 WRF microphysics schemes at 10 GHz.

468 At 19 GHz, all DDA habits produce excessive scattering for the WSM6 and WDM6  
469 simulations, where the dendrite and sector habits simulate the warmest TBs closest to



470 the observed reference TBs, and the thick hexagonal plates and the block, long and short  
471 hexagonal columns (not shown) are the most scattering habits, producing the coldest TBs,  
472 followed by the thin hexagonal plate and the rosettes (only the 6-b rosette is shown). On  
473 the other hand, all DDA habits in the THOM scheme simulations produce similar TB  
474 depressions to those observed. The large depression observed at 19 GHz in the WSM6/WDM6  
475 simulations is due to the high IWP graupel contents simulated by WRF. Note that due  
476 to the small brightness temperature depressions simulated using the THOM scheme, the  
477 signal coming from the lake at approximately  $-32.9^\circ$  can be observed at 19 GHz, while  
478 simulations using the WSM6/WDM6 schemes are dominated by excessive scattering and  
479 consequently cloud signals dominate all surface signals. Note that although the THOM  
480 scheme is predicting the largest amount of integrated snow content, it does not neces-  
481 sarily produce the largest brightness temperature depressions.

482 Similar conclusions can be drawn for the 37 GHz simulations. At 37 GHz, however,  
483 as expected, the sensibility to scattering increases and consequently TB depressions also  
484 increase. All habits, except the sector and dendrite habits, produced excessive scatter-  
485 ing with the WSM6 and the WDM6 schemes. Under the WDM6 scheme simulations, DDA  
486 habits show a warmer TBs compared to the WSM6 scheme. This is due to the strong  
487 graupel contents simulated by the WSM6 scheme. In the WSM6 and WDM6 schemes,  
488 sector and dendrite habits simulate comparable TBs to those observed, while the thick  
489 hexagonal plates and the block, long and short hexagonal columns (not shown) are the  
490 most scattering habits, producing larger TB depressions to those observed, followed by  
491 the thin hexagonal plate and the rosettes (only the 6-b rosette is shown). For the THOM  
492 scheme simulations, the DDA habits show a smaller spread in simulated TBs, and these  
493 TBs are all comparable to the reference observations, except for the 3-b, 4-b and 5-b rosettes  
494 (not shown) and the sector habit.

495 Simulations at 85 GHz, as expected, show an even higher sensitivity to scattering.  
496 In general, the combination of WSM6 and WDM6 and the DDA habits analysed follow  
497 the same sensitivities because they have the same particle size distribution, the same snow  
498 and graupel density ( $0.1$  and  $0.4$   $\text{kg}/\text{m}^3$ ), and similar snow and graupel column contents.  
499 In these schemes, and for all the frequencies analysed, the sector and dendrite habits scat-  
500 ter the least and produce TB depressions closest to the reference TMI observations. The  
501 thick hexagonal plates and the long, short and block hexagonal columns (not shown) scat-  
502 ter the most, followed by the thin hexagonal plate and rosettes (only the 6-b rosette is  
503 shown). These produce excessive scattering in comparison to the reference observations.  
504 As discussed in Section 3, the bulk DDA(THOM) scattering properties is different to the  
505 bulk DDA(WSM6/WDM6) scattering properties due to the different particle size dis-  
506 tributions and mass-size relationships (see discussion in Section 3). This is illustrated  
507 in Figure 7 for the 85 GHz channel simulations. For the THOM scheme simulations, con-  
508 trary to the WSM6 and WDM6 simulations, the thin hexagonal plate is simulating the  
509 warmer TBs (smallest TB depressions), while the sector habits are producing the cold-  
510 est temperatures (largest TB depressions).

511 MHS simulations at higher frequencies provide higher sensitivity to the scattering  
512 properties. Figure 8, similarly to Figure 7, focuses on a specific MHS scan from close to  
513 nadir to its outermost angle east, characterized by a large snow content in the WRF sim-  
514 ulations (see black line Figure 4g). This transect belongs to observations on the 6th De-  
515 cember at 17 UTC shown in Figure 2, where the system is in its developed stage. Fig-  
516 ure 8 shows the simulated brightness temperatures of MHS channels with the exception  
517 of the  $183\pm 3$  GHz, as it is very similar to the  $183\pm 1$  GHz due to its water vapour sen-  
518 sitivity, for the WSM6, WDM6 and THOM schemes. The bottom row of Figure 8 shows  
519 the corresponding integrated snow, graupel and rain contents simulated by the differ-  
520 ent WRF schemes and the outmost right column shows the corresponding reference MHS  
521 observations. MHS observations must be used as a reference and not as a direct com-



522 parison to the simulations due to differences in timing and spatial structure of the me-  
523 teorological fields modelled by WRF.

524 As expected the higher the window channel, the largest the brightness tempera-  
525 ture depressions. As analysed for the TMI transect, Figure 8 shows that for WSM6 and  
526 WDM6 simulations, the dendrite and sector habits are the least scattering habits, and  
527 for simulations with the THOM scheme, the dendrite and the thin hexagonal plates (and  
528 the thick hexagonal plates and the long, short and block hexagonal columns not shown),  
529 are the least scattering habits. The habits producing the largest brightness temperature  
530 depressions in the WSM6 and WDM6 schemes are the thick hexagonal plates and the  
531 long, short and block hexagonal columns (not shown), followed by the thin hexagonal  
532 plate and the rosettes (only the 6-b rosette is shown), as discussed for the TMI chan-  
533 nels simulated. In the THOM scheme, the coldest TBs are observed for the sector habits  
534 and the thin hexagonal plates as shown in Figure 8, and the thick hexagonal plates and  
535 the long, short and block hexagonal columns (not shown), also as discussed for the TMI  
536 channels.

537 As shown in Figure 7 for the TMI simulations, the THOM scheme MHS simula-  
538 tions in Figure 8 show that, in contrast to the WSM6 and WDM6 scheme simulations,  
539 the thin hexagonal plate is producing the smallest brightness temperature depressions  
540 and the sector habit is producing the largest brightness temperature depressions. This  
541 is a result of the equal mass approach and the schemes particle size distributions.

542 Note that simulations using the soft sphere approximation and with a Mie theory  
543 with the corresponding WRF microphysics parameterized densities are included in Fig-  
544 ure 8 (black dashed lines). The behaviour of the Mie sphere simulations compared with  
545 those of the DDA habits are very different with frequency, and are not scattering enough  
546 at large frequencies. Following *Liu* [2004], Mie theory can be used to reproduce the en-  
547 semble of the DDA database by adjusting the air fraction with frequency. This approach  
548 hence has no physical basis. It can be argued, however, that choosing one of the Liu habits  
549 to represent the highly complex and variable habit population is also problematic.

550 Figures 9 and 10 show a quantitative comparison of the simulated and observed  
551 brightness temperature distributions for the whole meteorological scene simulated for  
552 relevant TMI and MHS observations respectively. The statistical distributions of the bright-  
553 ness temperatures are shown for the observations (black line) and radiative transfer sim-  
554 ulations of a selected group of DDA habits (colored lines consistent with Figures 6, 7 and  
555 8). Note that only data over land, i.e., excluding coastal data and data over the ocean,  
556 is accounted in these distributions which are built with 5 K bins and where bins with  
557 less than 5 counts are neglected.

558 As expected, Figures 9 and 10 show that most departures between observations and  
559 simulations are associated with cloudy situations at low brightness temperatures. Fig-  
560 ure 9 shows that, as expected, simulations at 10 GHz show little sensitivity to scatter-  
561 ing. At the higher 19 GHz channel, the simulations start to show a larger sensitivity to  
562 the DDA habits. The simulations using the WDM6 scheme lead to excessive scattering  
563 at 19 and 37 GHz for all the habits shown. For the simulations with the WSM6 scheme,  
564 the thin hexagonal plate and the 6-b rosette show excessive scattering in comparison to  
565 observations at 37 and 89 GHz, while the sector and dendrite habits show a compara-  
566 ble distribution with those observed. Finally, simulations with the THOM scheme show  
567 comparable distributions to those observed for all DDA habits up to 37 GHz, while at  
568 89 GHz the thin hexagonal plate and the dendrite habits behave similarly to the obser-  
569 vations. Figure 10 shows further information to analyse the sensitivity to the choice of  
570 DDA habits using the higher frequency channels onboard MHS. Similarly to Figure 9,  
571 simulations with the WDM6/WSM6 scheme, and the thin hexagonal plate or the 6-b rosette  
572 show excessive scattering specially for the 89 and 157 GHz MHS frequency channels, while  
573 the sector habit produces a TB distribution closest to the observed distribution. Finally,



574 the simulations with the THOM scheme show that the sector and 6-b rosette produce  
575 excessive scattering, while the dendrite and thin hexagonal plate produce distributions  
576 closest to those observed. In general for the scene analysed, the dendrite habit performs  
577 best for all the schemes. Similar results were obtained by *Geer and Baordo* [2014] when  
578 analyzing the DDA shapes over land.

579 With the aim of analysing quantitatively the behaviour of the different DDA habits  
580 under the three different microphysics schemes, the chi-square test is used. The chi-square  
581 test is a verification method to evaluate how close the simulated distributions are to the  
582 observed distributions. Figure 11 and 12 show the relative residuals  $E_i$  computed for each  
583 bin following:

$$E_i = [X(i) - Y(i)] / \sqrt{X(i)}, \quad (5)$$

584 where  $X(i)$  and  $Y(i)$  are the relative frequencies of observations and simulations respec-  
585 tively for the  $i$ th bin of the TMI and MHS observations respectively. The histograms and  
586 the  $\chi^2 = \sum E_i^2$  values shown only take into account bins below 270 K (250 K for the  
587  $183 \pm 1$  GHz) in order to neglect clear sky pixels and focus on the cloudy contribution.  
588 Figure 11 and 12 further aid the analysis of Figure 9 and 10, to point at the performance  
589 of the simulations using the different DDA habits with the different microphysics schemes.  
590 The dendrite habits show low  $\chi^2$  value across the microphysics schemes. In the WSM6  
591 and WDM6 schemes, the sector snowflakes also perform well. The sector snowflakes, how-  
592 ever, show very high  $\chi^2$  values in the THOM scheme simulations. In the THOM scheme  
593 simulations, the thin hexagonal plates follow the dendrite habits in the low  $\chi^2$  values.

594 Finally, Figure 13 (Figure 14) shows TMI (MHS) observations in the first column,  
595 followed by the radiative transfer simulations using the dendrite habits to describe the  
596 scattering properties in the WSM6, WDM6 and THOM schemes (second, third and fourth  
597 columns respectively). Despite errors in the location and coverage of the spatial struc-  
598 tures of the cloudy fields modelled by WRF, the results depicted in Figure 13 shows that  
599 radiative transfer simulations using the WSM6 and the THOM microphysics schemes  
600 can be used to simulate the observed brightness temperature depressions provided spe-  
601 cial care is taken to represent the scattering properties of the snow and graupel species.  
602 At low microwave frequencies, Figure 13 shows that the WDM6 scheme leads to exces-  
603 sive scattering at  $>19$  GHz. Figure 14 shows good agreement between the three micro-  
604 physics schemes and MHS observations.

## 605 5 Extending the radiative transfer simulations to two additional MCS 606 events of interest

607 Two additional convective events in South Eastern South America are analysed in  
608 this section in order to further test the validity of the above drawn conclusions. The two  
609 events are observed over central Argentina on the 13 January 2011 and the 23 January  
610 2014, and microwave observations are available from SSMI/S at 2200 UTC and MHS at  
611 0200 UTC respectively. These observations are shown for the most scattering sensitive  
612 channels in the first and second rows of Figure 15 for SSMI/S and MHS for a relevant  
613 selection of instrument channels.

614 Figure 16 shows the integrated column contents in  $\text{kg/m}^2$  with a minimum thresh-  
615 old of  $0.05 \text{ kg/m}^2$ , simulated by WRF for these two scenes at the time of the available  
616 coincident observations. Figure 16 shows the strong sensitivity of the hydrometeor con-  
617 tents to the WRF microphysical parametrizations, as discussed in Section 2.2. Similarly  
618 to the WRF simulations analyzed in Section 2.2, Figure 16 shows that the WSM6 and  
619 the WDM6 schemes model similar hydrometeor mass loadings for the iced species (i.e.,  
620 snow, graupel and ice, not all shown), while the THOM scheme shows much higher snow  
621 contents. Similarly to the scene analysed in the previous section, the WSM6 simulates  
622 the largest amount of graupel content (not shown) followed by the WDM6 scheme. The  
623 THOM scheme produces very little graupel contents. Note that the two scenes analysed



624 in this section are comparable in IWPs with the case analysed in Section 4. Similarly  
625 to Section 3, it can also be said from Figures 15 and 16 that the microphysics schemes  
626 in WRF model the structure and location of the cloudy system fairly well for these two  
627 scenes too.

628 Radiative transfer simulations are performed for these two scenes in the same man-  
629 ner as described in Section 3 and the histograms of the simulated and observed bright-  
630 ness temperatures for the two scenes (not shown) are analysed. Analysing the scene on  
631 the 13 January 2011 which has coincident SSMI/S observations, it can be shown that  
632 at 19 GHz the radiative transfer simulations using all the DDA habits with the WSM6,  
633 WDM6 and THOM schemes, result in similar TBs. Unlike the scene analysed in Sec-  
634 tion 4, the WDM6 scheme in this scene does not show excessive scattering at 19 GHz.  
635 At 37 GHz, however, the WDM6 simulations show a pronounced large population of sim-  
636 ulations with brightness temperatures between 250 to 270 K for all habits. At 37 GHz,  
637 the WDM6 scheme simulations show that the thin hexagonal plates and the 6-b rosettes  
638 have the coldest brightness temperatures (largest TB depressions). These TB depres-  
639 sions are unrealistically large compared to the coincident observations. In the WSM6 sim-  
640 ulations, similarly to section 4, the thin hexagonal plate and the 6-b rosette habits are  
641 responsible for the coldest brightness temperatures, while the dendrite and sector snowflakes  
642 have warmer TBs and are closer to the observed brightness temperatures. The simulated  
643 THOM scheme brightness temperatures, on the other hand, show that all DDA habit  
644 simulations produce TBs that are very close to the observed TB distributions, as dis-  
645 cussed for the simulations in Section 4.

646 For frequencies above 37 GHz, i.e., 91V, 150H and 183±6H GHz, since there is a  
647 larger sensitivity to scattering, there is a larger sensitivity to the different habits. To aid  
648 this discussion, the relative residuals  $E_i$  are computed for this histograms in the same  
649 way as described in Section 4, and their  $\chi^2$  values shown in Figure 17(a). As shown in  
650 Section 4, the THOM scheme simulations with the thin hexagonal plate and the den-  
651 drite habits show the smallest  $\chi^2$  values, while in the WSM6/WDM6 the dendrite and  
652 sector snowflakes show the smallest  $\chi^2$  values. Similar conclusions are drawn for the scene  
653 with available coincident MHS observations, where the corresponding residuals and  $\chi^2$   
654 values calculated from the histograms of the brightness temperatures are shown in Fig-  
655 ure 17(b). Note that only the most sensitive channels to scattering are shown, i.e., 89  
656 GHz, 157 GHz and 190 GHz.

657 Finally, Figure 19 and 20 show that, as discussed for the MCS event simulated and  
658 analysed in Section 4, radiative transfer simulations using the WSM6 and the THOM  
659 microphysics schemes can be used to simulate the observed brightness temperature de-  
660 pressions using the dendrite DDA habits to represent the scattering properties of the snow  
661 and graupel species. In this scene, as discussed above, the WDM6 scheme is not observed  
662 to produce excessive scattering at low microwave frequencies, but is shown to produce  
663 warmer brightness temperatures than observed at MHS channels.

## 664 6 Conclusion

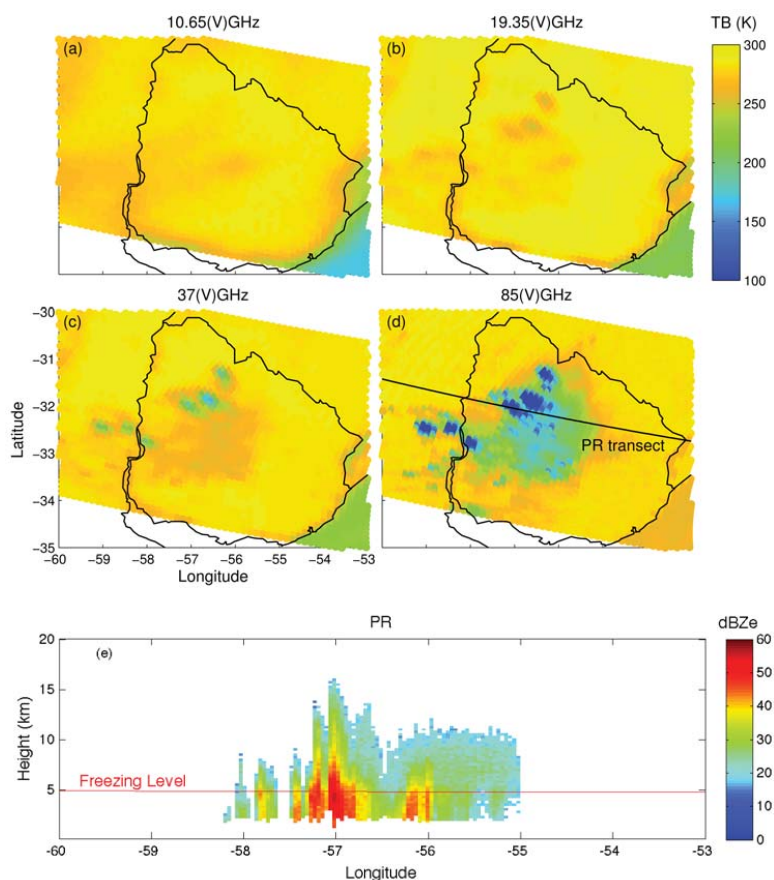
665 Three meteorological events of extreme deep moist convection, characteristic of South  
666 Easter South America, have been considered in the present study to conduct a direct com-  
667 parison between satellite-based simulated and observed microwave radiances, and to eval-  
668 uate three different WRF microphysical schemes. In order to do this, a research radi-  
669 ative transfer model, ARTS, has been coupled with the WRF model under the WSM6,  
670 WDM6 and THOM microphysical parametrizations. Since the simulation of passive mi-  
671 crowave radiances requires good knowledge of the scattering properties of frozen hydrom-  
672 eteors, the present study has further aimed at improving the understanding of frozen hy-  
673 drometeor optical properties and the characteristics of deep convection in the SESA re-  
674 gion. Bulk optical properties are computed by integrating the single scattering proper-



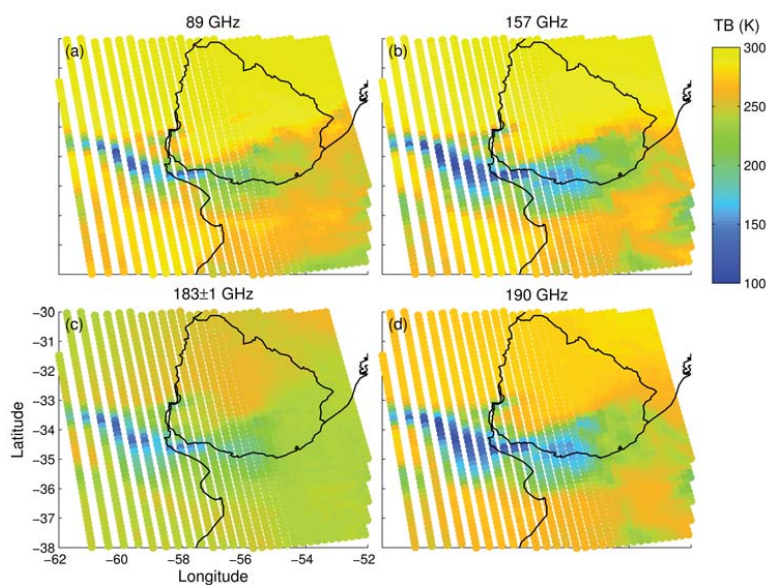
675 ties of particles across a given particle size distribution. While the particle size distri-  
676 bution of species is intrinsic to each WRF microphysics scheme, cloud resolving mod-  
677 els like WRF do not determine all of the parameters needed to determine the single scat-  
678 tering properties, and further assumptions are necessary. In this study the Liu (2008)  
679 DDA single scattering database, with 11 different iced habits, has been used to provide  
680 realistic scattering properties for snow and graupel species. In order to apply the opti-  
681 cal properties of the Liu (2008) DDA database to the hydrometeor species modelled by  
682 the WRF microphysics schemes in a consistent manner, the equal-mass approach is in-  
683 troduced. The equal mass approach consists in describing the optical properties of the  
684 WRF snow and graupel hydrometeors with the optical properties of habits in the DDA  
685 database whose dimensions might be different ( $D'_{max}$ ) but whose mass is conserved. The  
686 performance of the radiative transfer simulations have been evaluated by comparing the  
687 simulations with the available coincident microwave observations up to 190 GHz (with  
688 TMI, MHS, and SSMI/S). The systematic evaluation of WRF+ARTS radiative trans-  
689 fer simulations presents a tool to evaluate the representativity of the different WRF mi-  
690 crophysics schemes.

691 In the present study, a strong sensitivity of the hydrometeor column contents to  
692 the choice of WRF microphysics scheme has been shown. The WSM6 and the WDM6  
693 schemes model similar hydrometeor mass loadings for all iced species, while the THOM  
694 scheme shows higher snow contents. The WSM6 has been shown to simulate the largest  
695 amount of graupel contents followed by the WDM6 scheme, and finally the THOM scheme  
696 that produces very little graupel contents. An analysis of the domain-averaged vertical  
697 distribution of the hydrometeor contents, nonetheless, shows a comparable behaviour of  
698 the total ice phase (ice+snow+graupel) for the schemes analysed.

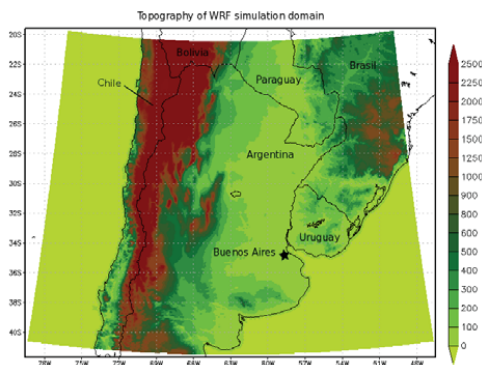
699 A direct comparison of the simulated and observed brightness temperatures shows  
700 that the microphysics schemes in WRF model the overall structure and location of the  
701 cloud system fairly well. The large sensibility to DDA habit choice shown in the simu-  
702 lated brightness temperatures, evidences the complexity in characterizing the frozen hy-  
703 drometeors scattering signal and the importance of improving our knowledge in the sub-  
704 ject. Although the present study has not aimed to search for the 'best' Liu habit, the  
705 statistical performance of the simulated brightness temperatures of the different Liu (2008)  
706 habits has been evaluated by analysing the histograms of the observed and simulated  
707 brightness temperatures, and using the chi-square test to evaluate how close the simu-  
708 lated distributions are to the observed distributions and hence the representativity of  
709 the different WRF microphysics schemes. The bulk scattering properties of the Liu (2008)  
710 habits are similar for the WSM6 and WDM6 schemes, but different to the THOM scheme.  
711 This is due to the different particle size distributions and mass-size relationships. This  
712 is reflected in the statistical analysis of the observed and simulated brightness temper-  
713 atures. For example, the thin hexagonal plates are shown to be one of the least scatter-  
714 ing habits in the THOM scheme simulations, but one of the most scattering in the WSM6/WDM6  
715 simulations. The opposite is shown for the sector habits. Nonetheless, disregarding the  
716 observed detailed spatial structures, an overall agreement is obtained between the simu-  
717 lated and the observed brightness temperatures, provided that special attention is taken  
718 when describing the optical properties of snow and graupel species. The dendrite and  
719 the thin hexagonal plate habits show the smallest  $\chi^2$  values for the THOM scheme WRF  
720 simulations, while the sector and dendrite habits show the the smallest  $\chi^2$  values for the  
721 WSM6 and WDM6 schemes.



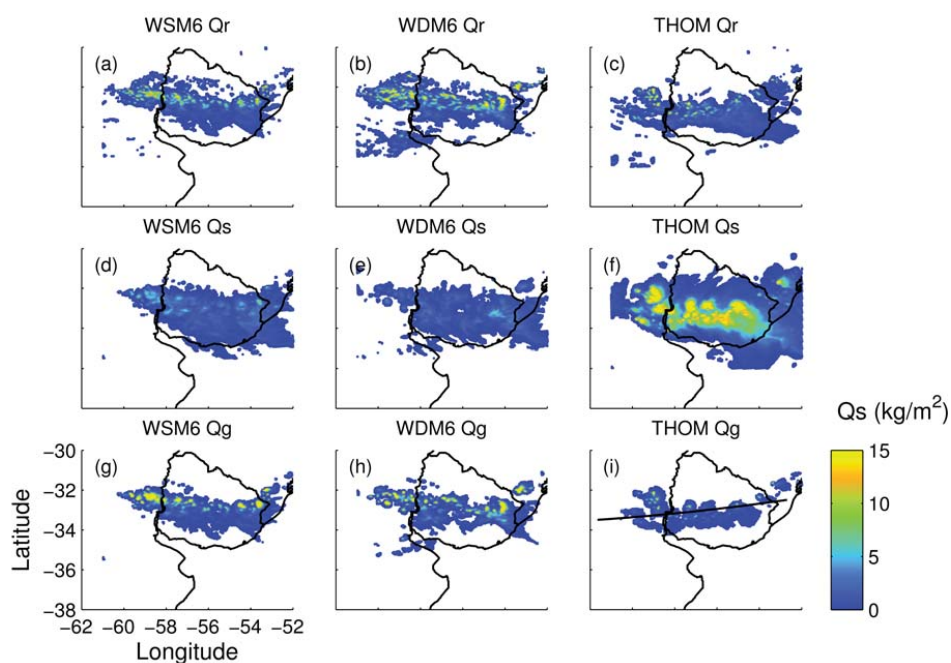
722 **Figure 1.** TMI observations on 6 December 2012 at 07:00 UTC for AN MCS event of interest  
723 in the present study. Note that the horizontally polarized channels and the 22V GHz channel ob-  
724 servations are not shown. The solid black line in 1(d) represents the location of the PR transect  
725 shown in 1(e).



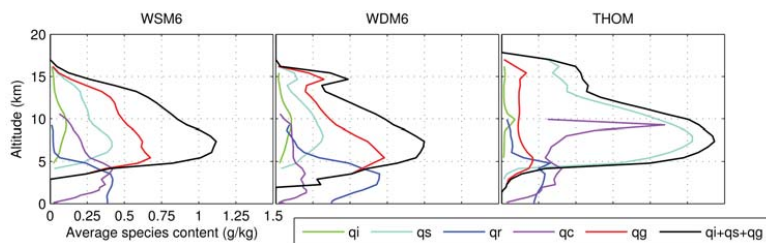
726 **Figure 2.** MHS observations on 6 December 2012 at 19:00 UTC for an MCS event of interest  
727 in the present study. Note that the  $183\pm 3$  GHz channel is not shown.



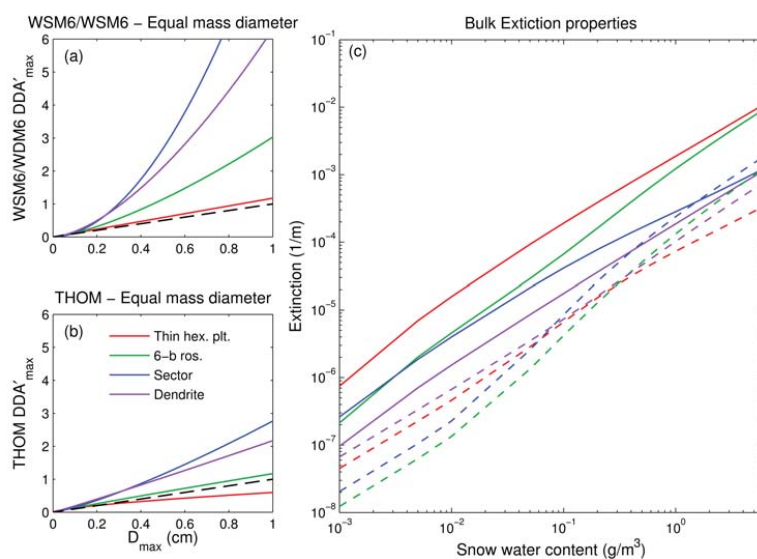
728 **Figure 3.** The geographical domain used in WRF model runs illustrated by the topography of  
729 the region in meters.



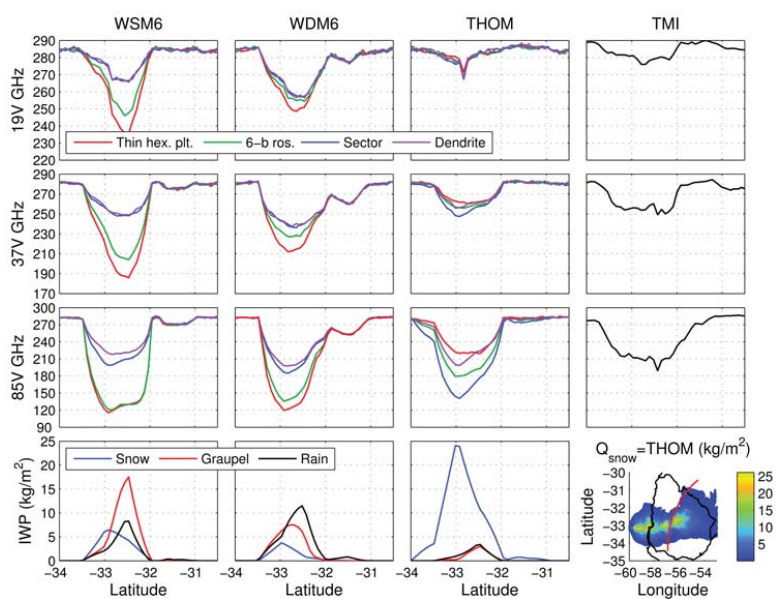
730 **Figure 4.** The integrated column contents in  $\text{kg/m}^2$  for rain, snow and graupel, as simulated  
 731 by the WRF microphysics options WSM6, WDM6 and THOM, at 1900 UTC with a  $0.05 \text{ kg/m}^2$   
 732 minimum threshold. Note that cloud water and cloud ice are not shown. The black solid line in  
 733 4(i) represents an MHS transect explored in Section 4.



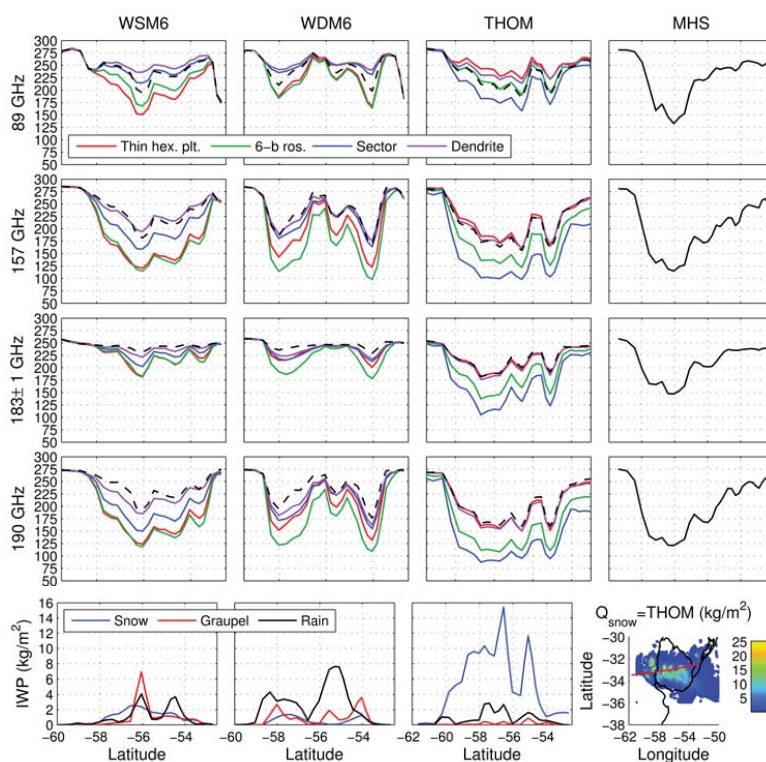
734 **Figure 5.** The domain-averaged vertical species content as modelled by WRF between 18:00  
 735 and 19:00 UTC by the WSM6, WDM6, and THOM microphysics options. Units are in  $\text{g/kg}$  for  
 736 all species, and the domain-average is calculated from Figure 4.



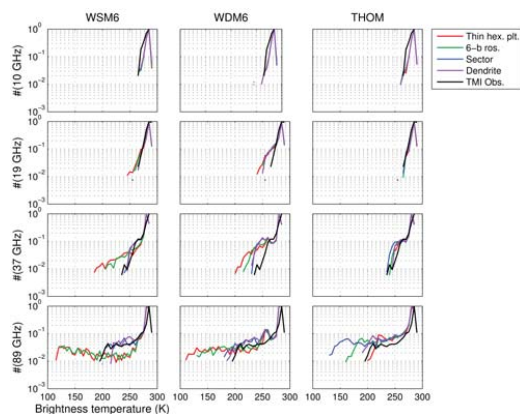
737 **Figure 6.** Left: The corresponding equal mass DDA habit size calculated from Equation 3 for  
 738 WRF (a) WSM6 and WDM6 and (b) THOM schemes. (c) Right: The bulk scattering properties,  
 739 i.e., the extinction coefficient for the WSM6 and WDM6 and the THOM schemes as a function  
 740 of snow water content at 150 GHz at 263 K. The bulk optical properties have been computed  
 741 by integrating the scattering properties of all equal mass Liu [2008] particle habits over the size  
 742 distributions of interest.



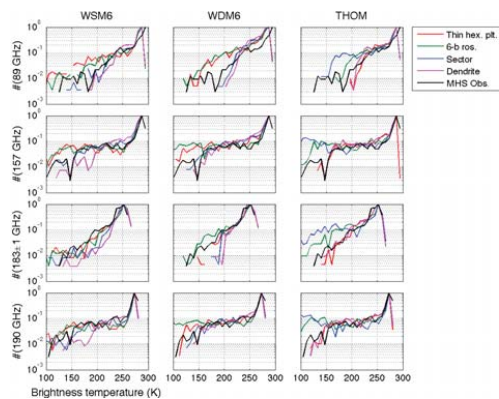
743 **Figure 7.** The simulated brightness temperatures for the TMI 19V, 37V, 85V GHz channels  
 744 along a specific transect of interest shown in the bottom right panel, using selected Liu (2008)  
 745 DDA habits (see legend) and the WSM6, WDM6 and THOM WRF schemes (the first 3 columns)  
 746 and the observed brightness temperatures (in black in the last column). The corresponding inte-  
 747 grated mass contents of snow, graupel and rain are shown in the bottom row. Note that the  
 748 bottom right panel shows the column integrated WRF (THOM) snow mass content for the whole  
 749 scene together with a solid red line to illustrate the location of the transect of interest.



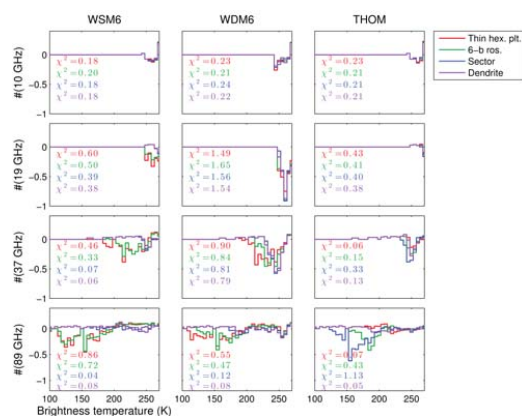
750 **Figure 8.** Similarly to Figure 7, the simulated brightness temperatures for the 89, 157, 183±1  
 751 and 190 GHz MHS channels along the transect of interest shown in Figure 4(i) using a selection  
 752 of Liu (2008) DDA habits and the WSM6, WDM6 and THOM WRF schemes (in the first three  
 753 columns). The last column shows reference MHS observations for the transect in solid black lines.  
 754 The corresponding integrated mass contents of snow, graupel and rain are shown in the bottom  
 755 row. Note that the bottom right panel shows the column integrated WRF (THOM) snow mass  
 756 content for the whole scene together with a solid red line to illustrate the location of the transect  
 757 of interest.



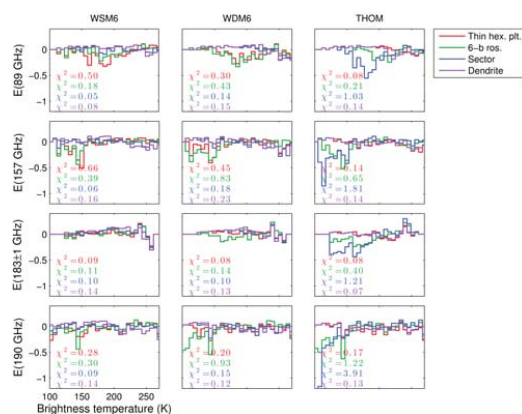
758 **Figure 9.** The observed (solid black line) and simulated (solid colored lines) TMI bright-  
759 ness temperature distributions (built with 5 K bins and where bins with less than 5 counts are  
760 neglected).



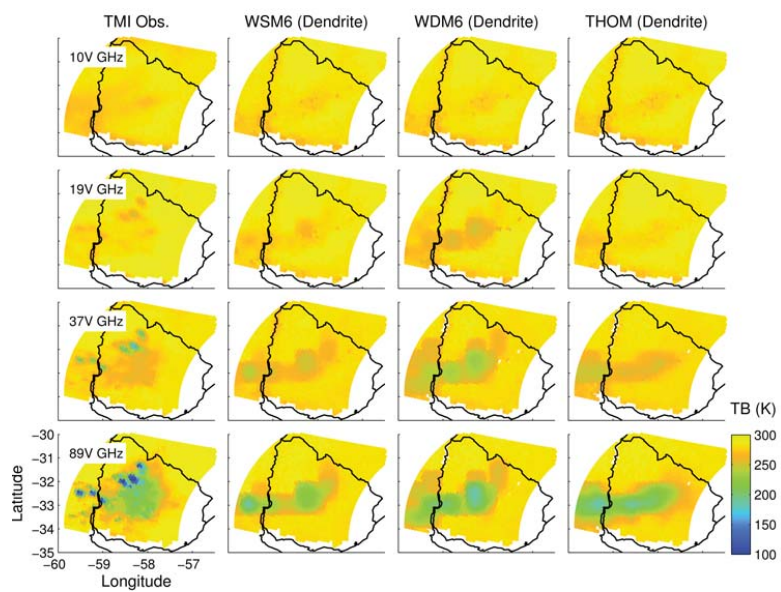
761 **Figure 10.** The observed (solid black line) and simulated (solid colored lines) MHS bright-  
762 ness temperature distributions (built with 5 K bins and where bins with less than 5 counts are  
763 neglected).



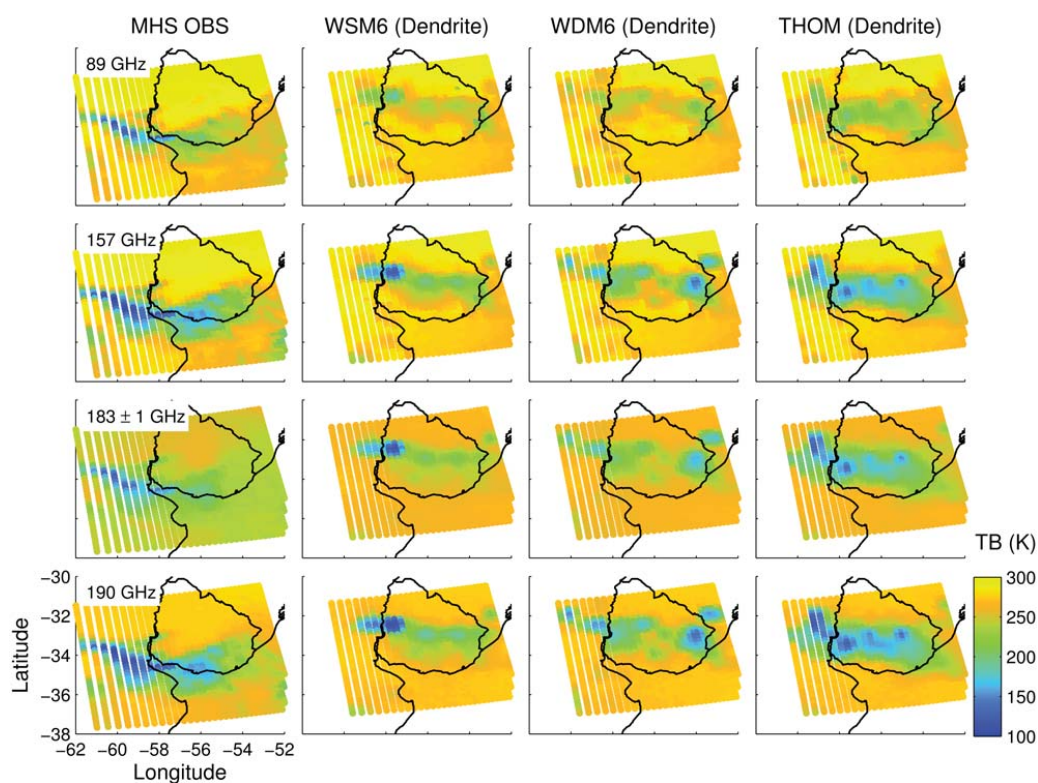
764 **Figure 11.** The simulated (solid colored lines) residuals of the Chi-squared test for the TMI  
 765 brightness temperature distributions. Note that the  $\chi^2$  value is included for each of the DDA  
 766 habit simulated distributions calculated from all temperature bins below 270 K.



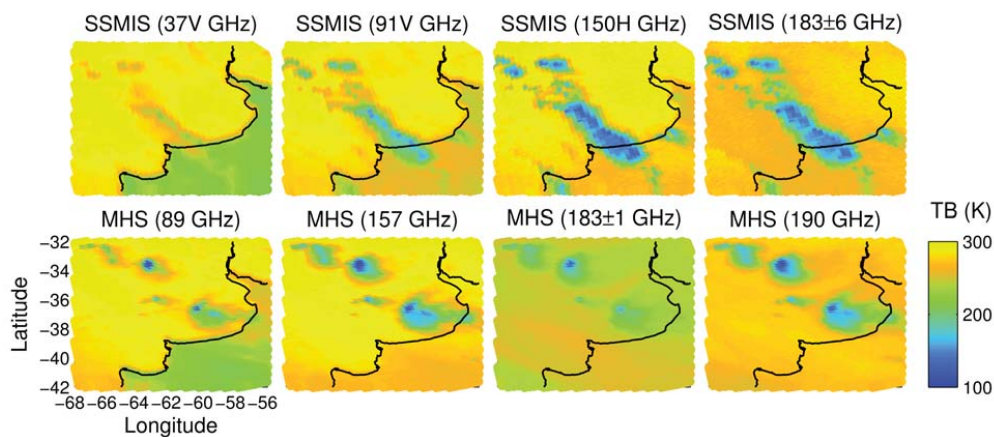
767 **Figure 12.** The simulated (solid colored lines) residuals of the Chi-squared test for the MHS  
 768 brightness temperature distributions. Note that the  $\chi^2$  value is included for each of the DDA  
 769 habit simulated distributions calculated from all temperature bins below 270 K (250 K for the  
 770  $183\pm 1$  GHz channel).



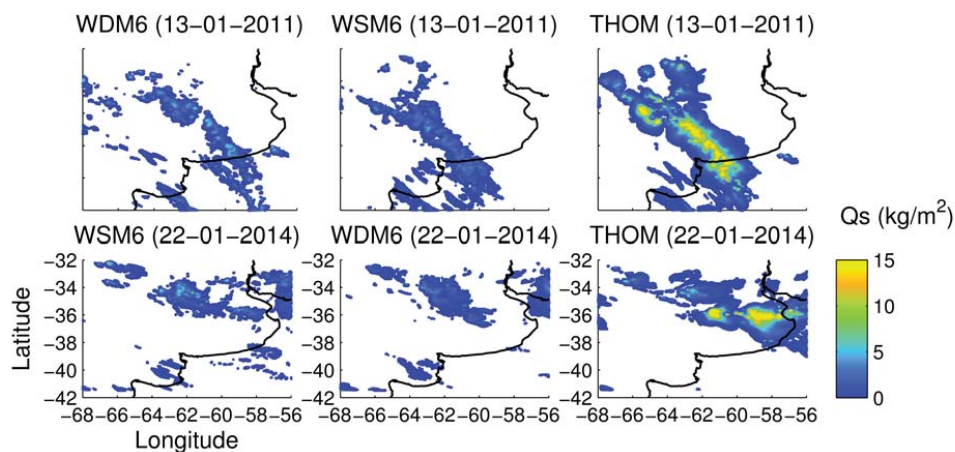
771 **Figure 13.** TMI observations at 10V, 19V, 37V and 89V GHz (first column), as compared to  
772 the corresponding radiative transfer simulations using the dendrite habits for the WSM6, WDM6  
773 and THOM scheme simulations.



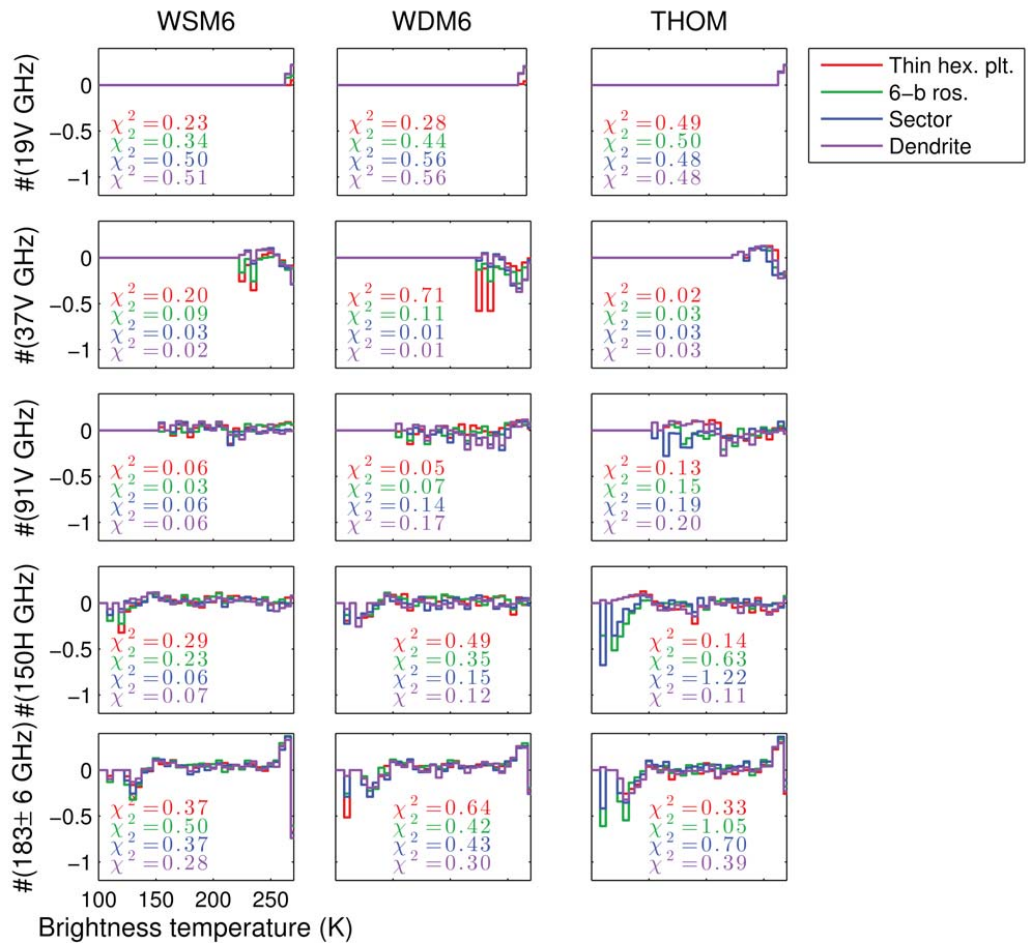
774 **Figure 14.** MHS observations at 89, 157, 183±1 and 190 GHz, as compared to the corre-  
775 sponding radiative transfer simulations using the dendrite habits for the WSM6, WDM6 and  
776 THOM scheme simulations.



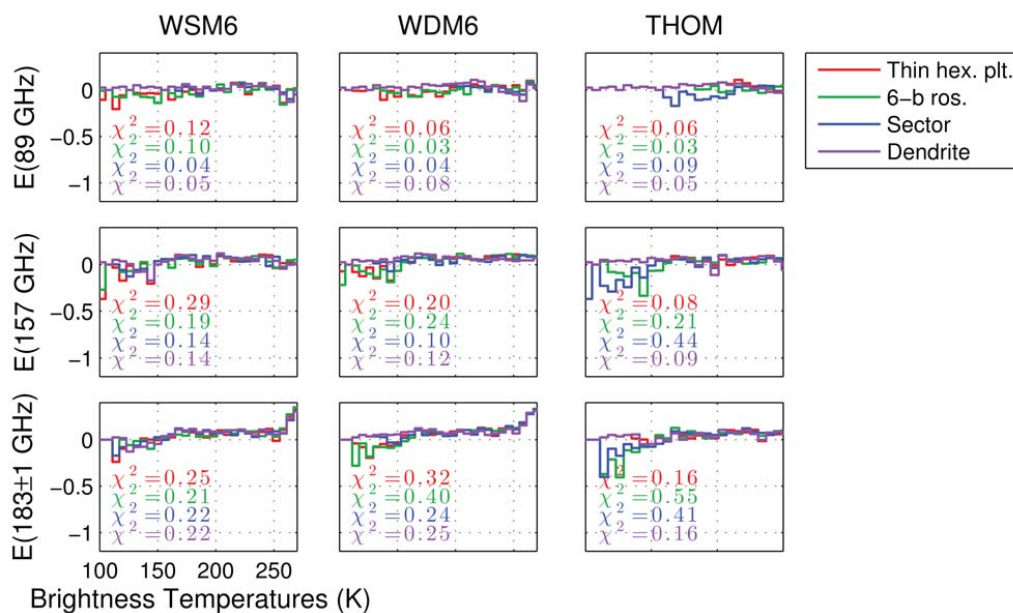
777 **Figure 15.** Coincident microwave observations for two MCS events of interest. Top row: observed  
 778 brightness temperatures for selected SSMI/S channels over South Easter South America  
 779 on the 13 January 2011 at 22 UTC. Bottom row: observed brightness temperatures for selected  
 780 MHS channels over South Easter South America on the 23 January 2014 at 2 UTC.



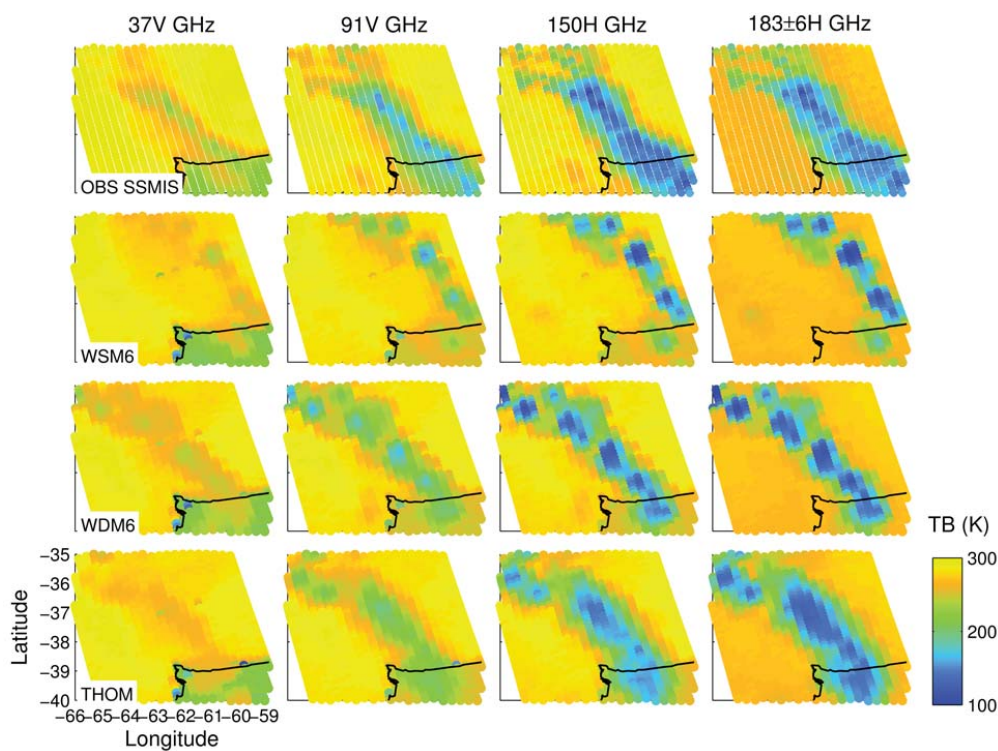
781 **Figure 16.** The integrated column contents in  $\text{kg/m}^2$  for snow as simulated by the WRF mi-  
 782 crophysics options WSM6, WDM6 and THOM, on the 13 January 2011 at 22 UTC (top row) and  
 783 on the 23 January 2014 at 2 UTC (bottom row), with a  $0.05 \text{ kg/m}^2$  minimum threshold



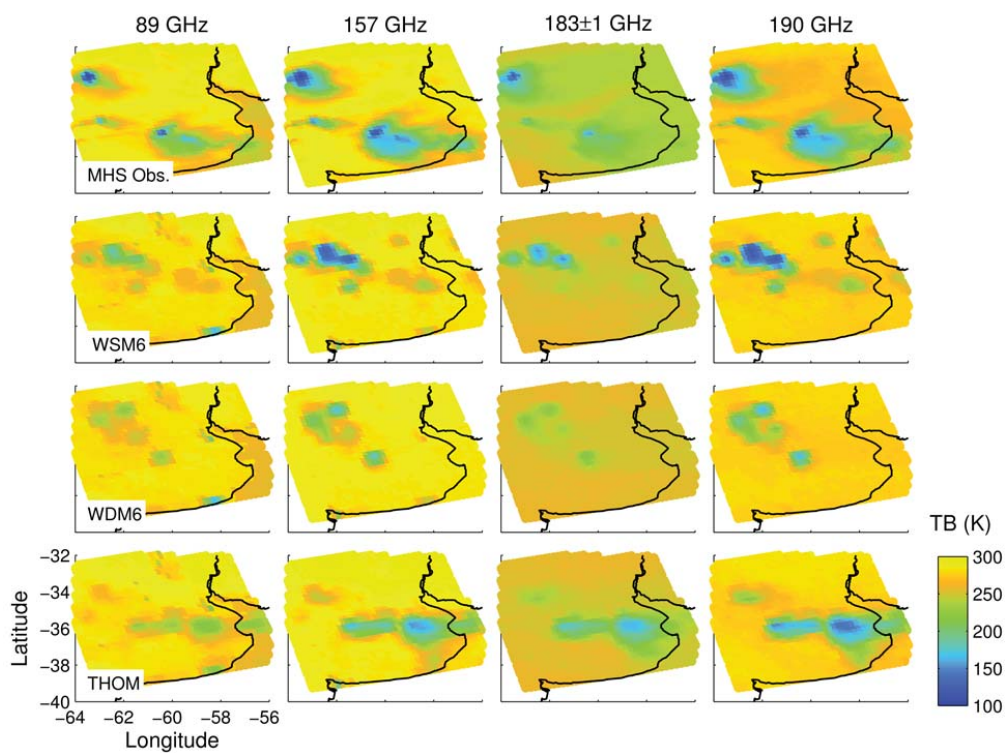
784 **Figure 17.** The simulated (solid colored lines) residuals of the Chi-squared test for the simu-  
 785 lated SSMI/S 19V, 37V, 91V, 150H and 183±6 GHz channels for the MCS events on the 13  
 786 January 2011 at 22 UTC. Note that the  $\chi^2$  value is included for selected DDA habit simulated  
 787 distributions calculated from all temperature bins below 270 K.



788 **Figure 18.** The simulated (solid colored lines) residuals of the Chi-squared test for the simu-  
 789 lated MHS 89, 157 and 183±1 GHz channels for the MCS events on the 13 January 2011 at 22  
 790 UTC. Note that the  $\chi^2$  value is included for selected DDA habit simulated distributions calcu-  
 791 lated from all temperature bins below 270 K and 250 K for the 183±1 GHz channel).



792 **Figure 19.** SSMI/S observations, as compared to the corresponding radiative transfer simulations using the dendrite habits for the WSM6, WDM6 and THOM scheme simulations for the 13  
793 January 2011 event analysed.  
794



795 **Figure 20.** MHS observations, as compared to the corresponding radiative transfer simula-  
796 tions using the dendrite habits for the WSM6, WDM6 and THOM scheme simulations for the 23  
797 January 2014 event analyzed.



798

**Table 1.** Overview of the *Liu* [2008] database

Habit	Range of max dimension ( $\mu\text{m}$ )	a	b
Long hexagonal column	121 - 4835	37.09	3.00
Short hexagonal column	83 - 3304	116.12	3.00
Block hexagonal column	66 - 2532	229.66	3.00
Thick hexagonal column	81 - 3246	122.66	3.00
Thin hexagonal column	127 - 5059	32.36	3.00
3-bullet rosette	50 - 10000	0.32	2.37
4-bullet rosette	50 - 10000	0.06	2.12
5-bullet rosette	50 - 10000	0.07	2.12
6-bullet rosette	50 - 10000	0.09	2.13
Sector snowflake	50 - 10000	0.002	1.58
Dendrite snowflake	75 - 12454	0.01	1.90



799

**Table 2.** The WRF parametrizations used

Physics	Parametrization
Microphysics	WRF Single-Moment 6 (WSM6; <i>Hong and Lim</i> [2006]) WRF Double-Moment 6 (WDM6, <i>Hong et al.</i> [2010]) Thompson (THOM, <i>Thompson et al.</i> [2008])
Long wave radiation	RRTM [ <i>Mlawer et al.</i> , 1997]
Short wave radiation	Dudhia [ <i>Dudhia</i> , 1989]
Surface-layer exchange coefficient	Monin-Obukhov (Janjic Eta) scheme
Surface processes	Noah LSM [ <i>Chen and Dudhia</i> , 2001]
PBL	MYJ Janjic [ <i>Janjic</i> , 1994]



800 **Acknowledgments**

801 This research was funded by the CNRS LEFE/IMAGO program. The authors would like  
802 to express their gratitude to the ARTS community for developing and maintaining an  
803 open source distribution

804 **References**

- 805 Altinger de Schwarzkopf, M. L., and G. Necco (1988), Climatología de los efectos  
806 de la conveccion severa en la republica argentina, Ph.D. thesis, Universidad de  
807 Buenos Aires (UBA). Facultad de Ciencias Exactas y Naturales (FyCEN). Doctor  
808 en Ciencias Meteorologicas.
- 809 Baran, A. J. (2012), From the single-scattering properties of ice crystals to climate  
810 prediction: A way forward, *Atmospheric Research*, 112, 45–69.
- 811 Buehler, S., N. Courcoux, and V. John (2006), Radiative transfer calculations for  
812 a passive microwave satellite sensor: Comparing a fast model and a line-by-line  
813 model, *Journal of Geophysical Research: Atmospheres*, 111(D20).
- 814 Chaboureaud, J.-P., N. Söhne, J.-P. Pinty, I. Meirold-Mautner, E. Defer, C. Prigent,  
815 J. R. Pardo, M. Mech, and S. Crewell (2008), A midlatitude precipitating cloud  
816 database validated with satellite observations, *Journal of Applied Meteorology and  
817 Climatology*, 47(5), 1337–1353.
- 818 Chen, F., and J. Dudhia (2001), Coupling an advanced land surface-hydrology model  
819 with the penn state-near mm5 modeling system. part i: Model implementation  
820 and sensitivity, *Monthly Weather Review*, 129(4), 569–585.
- 821 Davis, C., K. Evans, S. Buehler, D. Wu, and H. Pumphrey (2007), 3-d polarised  
822 simulations of space-borne passive mm/sub-mm midlatitude cirrus observations: a  
823 case study, *Atmospheric Chemistry and Physics*, 7(15), 4149–4158.
- 824 Doherty, A., T. Sreerekha, U. O’Keeffe, and S. English (2007), Ice hydrometeor  
825 microphysical assumptions in radiative transfer models at amsu-b frequencies,  
826 *Quarterly Journal of the Royal Meteorological Society*, 133(626), 1205–1212.
- 827 Draine, B. T., and P. J. Flatau (1994), Discrete-dipole approximation for scattering  
828 calculations, *JOSA A*, 11(4), 1491–1499.
- 829 Dudhia, J. (1989), Numerical study of convection observed during the winter mon-  
830 soon experiment using a mesoscale two-dimensional model, *Journal of the Atmo-  
831 spheric Sciences*, 46(20), 3077–3107.
- 832 Eriksson, P., S. Buehler, C. Davis, C. Emde, and O. Lemke (2011), Arts, the at-  
833 mospheric radiative transfer simulator, version 2, *Journal of Quantitative Spec-  
834 troscopy and Radiative Transfer*, 112(10), 1551–1558.
- 835 Eriksson, P., M. Jamali, J. Mendrok, and S. Buehler (2015), On the microwave opti-  
836 cal properties of randomly oriented ice hydrometeors, *Atmospheric Measurement  
837 Techniques*, 8(5), 1913–1933.
- 838 Field, P., R. Hogan, P. Brown, A. Illingworth, T. Choullarton, and R. Cotton (2005),  
839 Parametrization of ice-particle size distributions for mid-latitude stratiform cloud,  
840 *Quarterly Journal of the Royal Meteorological Society*, 131(609), 1997–2017.
- 841 Galligani, V., C. Prigent, E. Defer, C. Jimenez, P. Eriksson, J. Pinty, and  
842 J. Chaboureaud (2014), Meso-scale modeling and radiative transfer simulations  
843 of a snowfall event over france at microwaves for passive and active modes and  
844 evaluation with satellite observations., *Atmospheric Measurement Techniques  
845 Discussions*, 7(7).
- 846 Geer, A., and F. Baordo (2014), Improved scattering radiative transfer for frozen  
847 hydrometeors at microwave frequencies, *Atmospheric Measurement Techniques*,  
848 7(6), 1839–1860.
- 849 Goodman, S. J., J. Blakeslee, R., W. J. Koshak, D. Mach, J. Bailey, D. Buechler,  
850 L. Carey, C. Schultz, M. Bateman, E. McCaul, et al. (2013), The goes-r geosta-  
851 tionary lightning mapper (glm), *Atmospheric Research*, 125, 34–49.



- 852 Hong, S.-Y., and J.-O. J. Lim (2006), The wrf single-moment 6-class microphysics  
853 scheme (wsm6), *J. Korean Meteor. Soc.*, *42*(2), 129–151.
- 854 Hong, S.-Y., K.-S. S. Lim, Y.-H. Lee, J.-C. Ha, H.-W. Kim, S.-J. Ham, and J. Dud-  
855 hia (2010), Evaluation of the wrf double-moment 6-class microphysics scheme for  
856 precipitating convection, *Advances in Meteorology*, *2010*.
- 857 Janjic, Z. I. (1994), The step-mountain eta coordinate model: Further developments  
858 of the convection, viscous sublayer, and turbulence closure schemes, *Monthly*  
859 *Weather Review*, *122*(5), 927–945.
- 860 Kim, J.-H., D.-B. Shin, and C. Kummerow (2013), Impacts of a priori databases us-  
861 ing six wrf microphysics schemes on passive microwave rainfall retrievals, *Journal*  
862 *of Atmospheric and Oceanic Technology*, *30*(10), 2367–2381.
- 863 Kulie, M. S., R. Bennartz, T. J. Greenwald, Y. Chen, and F. Weng (2010), Uncer-  
864 tainties in microwave properties of frozen precipitation: Implications for remote  
865 sensing and data assimilation, *Journal of the Atmospheric Sciences*, *67*(11), 3471–  
866 3487.
- 867 Kummerow, C., W. Barnes, T. Kozu, J. Shiue, and J. Simpson (1998), The tropical  
868 rainfall measuring mission (trmm) sensor package, *Journal of atmospheric and*  
869 *oceanic technology*, *15*(3), 809–817.
- 870 Leinonen, J., S. Kneifel, D. Moisseev, J. Tyynelä, S. Tanelli, and T. Nousiainen  
871 (2012), Evidence of nonspheroidal behavior in millimeter-wavelength radar obser-  
872 vations of snowfall, *Journal of Geophysical Research: Atmospheres*, *117*(D18).
- 873 Liebe, H. J., G. A. Hufford, and T. Manabe (1991), A model for the complex per-  
874 mittivity of water at frequencies below 1 thz, *International Journal of Infrared*  
875 *and Millimeter Waves*, *12*(7), 659–675.
- 876 Lim, K.-S. S., and S.-Y. Hong (2010), Development of an effective double-moment  
877 cloud microphysics scheme with prognostic cloud condensation nuclei (ccn) for  
878 weather and climate models, *Monthly weather review*, *138*(5), 1587–1612.
- 879 Liu, G. (2004), Approximation of single scattering properties of ice and snow parti-  
880 cles for high microwave frequencies, *Journal of the atmospheric sciences*, *61*(20),  
881 2441–2456.
- 882 Liu, G. (2008), A database of microwave single-scattering properties for nonspherical  
883 ice particles, *Bulletin of the American Meteorological Society*, *89*(10), 1563.
- 884 Magono, C. (1965), Aerodynamic studies of falling snowflakes., *J. Meteorol. Soc.*  
885 *Japan*, *43*, 139–147.
- 886 Mätzler, C. (2006), *Thermal microwave radiation: applications for remote sensing*,  
887 vol. 52, Iet.
- 888 Maxwell-Garnett, J. (1906), Colours in metal glasses, in metallic films, and in metal-  
889 lic solutions. ii, *Philosophical Transactions of the Royal Society of London. Series*  
890 *A, Containing Papers of a Mathematical or Physical Character*, pp. 237–288.
- 891 Meirold-Mautner, I., C. Prigent, E. Defer, J. R. Pardo, J.-P. Chaboureau, J.-P.  
892 Pinty, M. Mech, and S. Crewell (2007), Radiative transfer simulations using  
893 mesoscale cloud model outputs: Comparisons with passive microwave and in-  
894 frared satellite observations for midlatitudes, *Journal of the atmospheric sciences*,  
895 *64*(5), 1550–1568.
- 896 Melsheimer, C., C. Verdes, S. Buehler, C. Emde, P. Eriksson, D. Feist, S. Ichizawa,  
897 V. John, Y. Kasai, G. Kopp, et al. (2005), Intercomparison of general purpose  
898 clear sky atmospheric radiative transfer models for the millimeter/submillimeter  
899 spectral range, *Radio science*, *40*(1).
- 900 Mezher, D. M., R., and V. Barros (2012), Climatology of hail in argentina, *Atmo-*  
901 *spheric research*, *114*, 70–82.
- 902 Mlawer, E. J., S. J. Taubman, P. D. Brown, M. J. Iacono, and S. A. Clough (1997),  
903 Radiative transfer for inhomogeneous atmospheres: Rrtm, a validated correlated-k  
904 model for the longwave, *Journal of Geophysical Research: Atmospheres*, *102*(D14),  
905 16,663–16,682.



- 906 Morrison, C. J. A., H., and V. Khvorostyanov (2005), A new double-moment mi-  
907 crophysics parameterization for application in cloud and climate models. part i:  
908 Description, *Journal of the Atmospheric Sciences*, 62(6), 1665–1677.
- 909 Prigent, C., F. Aires, D. Wang, S. Fox, and C. Harlow (2016), Sea surface emissivity  
910 parameterization from microwaves to millimeter waves, *Quarterly Journal of the*  
911 *Royal Meteorological Society*.
- 912 Salio, P., M. P. Hobouchian, Y. G. Skabar, and D. Vila (2015), Evaluation of high-  
913 resolution satellite precipitation estimates over southern south america using a  
914 dense rain gauge network, *Atmospheric Research*, 163, 146–161.
- 915 Saunders, R., P. Rayer, P. Brunel, A. Von Engel, N. Bormann, L. Strow, S. Han-  
916 non, S. Heilliette, X. Liu, F. Miskolczi, et al. (2007), A comparison of radiative  
917 transfer models for simulating atmospheric infrared sounder (airs) radiances,  
918 *Journal of Geophysical Research: Atmospheres*, 112(D1).
- 919 Silva Dias, M. A. F. (2011), An increase in the number of tornado reports in brazil,  
920 *Weather, Climate, and Society*, 3(3), 209–217.
- 921 Skamarock, W. C., and J. B. Klemp (2008), A time-split nonhydrostatic atmospheric  
922 model for weather research and forecasting applications, *Journal of Computational*  
923 *Physics*, 227(7), 3465–3485.
- 924 Thompson, G., P. R. Field, R. M. Rasmussen, and W. D. Hall (2008), Explicit fore-  
925 casts of winter precipitation using an improved bulk microphysics scheme. part  
926 ii: Implementation of a new snow parameterization, *Monthly Weather Review*,  
927 136(12), 5095–5115.
- 928 Wang, D., C. Prigent, F. Aires, and C. Jimenez (2016), A statistical retrieval of  
929 cloud parameters for the millimeter wave ice cloud imager on board metop-sg,  
930 *IEEE Access*.
- 931 Zipser, E. J., D. J. Cecil, C. Liu, S. W. Nesbitt, and D. P. Yorty (2006), Where are  
932 the most intense thunderstorms on earth?, *Bulletin of the American Meteorological*  
933 *Society*, 87(8), 1057.